Review

Radiation induced plasmonic nanobubbles: fundamentals, applications and prospects

Yifan Zhang, Wei An*, Chang Zhao and Qingchun Dong

College of Mechanical Engineering, Tongji University, Shanghai, P.R. China

* Correspondence: Email: anwei@tongji.edu.cn.

Abstract: When plasmonic nanoparticles (PNPs) are illuminated by a light source with a plasmon frequency, an intensive localized surface plasmon resonance (LSPR) effect can be excited, which causes an obvious enhancement of the local electric field around the PNPs. The light energy is converted into heat by the PNPs, causing a gradual increase in the temperature of the media around these PNPs. Under the induction of radiation, the heat generated by PNPs vaporizes the surrounding water, and under the combined effect of the local electric field, plasmonic nanobubbles (PNBs) are generated. After that, PNBs will continue to grow, which is mainly caused by the influx of dissolved gas from the surrounding water. With the growth of PNBs, PNB-induced micro convection and some unique nonlinear changes of optical properties can be observed. Since the size, location and lifetime of PNBs can be flexibly controlled by adjusting the parameters of the light source, PNBs have been widely used in several emerging applications such as microfluidic manipulations, medical drug delivery and cell therapy. In this review, we first introduce the physical mechanism of PNB generation and discuss the micro convection and optical nonlinearity caused by PNBs. In addition, we demonstrate the nucleation mechanism and the growth kinetics of PNBs. Then we review the PNBs-based applications in microfluid flow control, particle manipulation, optical property tuning, medical drug delivery and cancer therapy. Finally, we summarize the current challenges of this field and propose an outlook for future developments.

Keywords: nanoparticles; localized surface plasmon resonance; plasmonic nanobubbles

---

Nomenclature: AuNP: gold nanoparticle; CW: continuous wave; GNF: gold nanoisland film; LSPR: localized surface plasmon resonance; NP: nanoparticle; PL: pulsed laser; PNB: plasmonic nanobubbles; PNF: plasmonic fluid; PNP: plasmonic nanoparticle

1. Introduction

With the rapid progress in nanoscience, the comprehensive manipulation of light (across the entire visible and near-infrared regions of the solar spectrum) has been realized at the nanoscale, which has also stimulated the vigorous development of various emerging technologies [1,2]. Because the size of plasmonic nanoparticles (PNPs) is in the same order of magnitude as the wavelength of light, the fine-tuning of the radiation properties of nanoparticles (NPs) can be easily achieved by changing the morphology, size, material, and aggregation of particles [3,4]. When PNPs are illuminated by a light source with a plasmon resonance frequency, efficient photo-induced heating can be produced and diffused to the surrounding liquid [5,6]. Combined with the enhanced local electric field induced by the LSPR effect, plasmonic nanobubbles (PNBs) can be generated [7,8]. The generation of PNBs creates the inhomogeneity in temperature, density and particle concentration in the fluid, which is not only spatially dependent, but also dynamic in time [9]. Due to the non-uniform and non-linear changes in various physical fields, many unique optical and mechanical properties appear with the generation and growth of PNBs [10,11]. These unique physical properties make PNB great potential in various applications. For example, in the field of microfluidic control, PNB can act as a physical valve to control the flow of microfluids [12], and PNB-induced Marangoni convection can be used to manipulate fluids [13] or particles [14]. In the optics field, PNB can be taken as an adjustable lens to guide the propagation of surface waves [15]. In the biomedical field, PNB can be used for medical drug delivery [16] and cancer treatment [17].

The advantages of PNBs in different applications are reflected in two aspects: one is the adjustable and smaller bubble size; the other is the size, position and lifetime of PNBs can be easily controlled remotely by adjusting the light source parameters [18]. However, these two advantages also pose some difficulties for the research and application of PNBs at the same time. With the increasing accuracy of PNB manipulation, it is particularly important to a comprehensive analysis of the generation mechanism and development process of PNB. Although several review papers on PNB applications have been published [7,19], these papers always focus on applications and problems within different fields but lack a comprehensive summary of the relevant mechanism. To our knowledge, there is no systematic review on the mechanism of PNB generation and development.

In this review, we begin with the physical mechanism of localized surface plasmon resonance (LSPR), and electric field enhancement and photothermal effect induced by the LSPR effect. Next, we demonstrate the nucleation mechanism and the development of PNBs mediated by heat and plasma. Then, we discuss the micro convection caused by PNBs and highlight the importance of optical nonlinearity to radiative transfer. Further, we review the PNBs-based applications reported in recent studies. Finally, we summarize the current challenges of this field and raise some issues of concern. The framework structure of this review is shown in Figure 1.
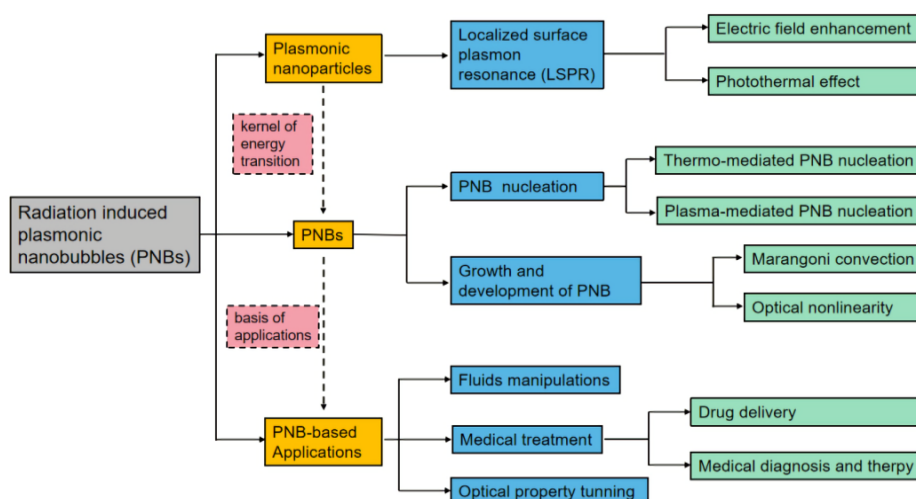
Figure 1. Schematic diagram of the research flow of the current study.

2. Plasmonic nanoparticle: the kernel of energy transition

2.1. Localized surface plasmon resonance

PNPs are nanoparticles that exhibit very strong light absorption and scattering due to the collective excitations of the conduction electrons known as localized surface plasmon resonance (LSPR) [20]. As shown in Figure 2, LSPR is a charge mismatch formed by the conduction electrons (or electron holes) in a metal (or semiconductor) under the irradiation of an incident electromagnetic wave [21], resulting in the oscillation phenomenon of the localized field on the surface of the particle, which rises and falls periodically with the fluctuation of the incident radiation. For the PNB generation process, PNPs are indispensable for light energy to be absorbed, transformed and generate heat and plasma, which provides energy for PNB nucleation. Thus, accurate and precise quantification of the energy absorbed and transformed by PNPs is essential for the kaleidoscopic applications based on the LSPR effect.
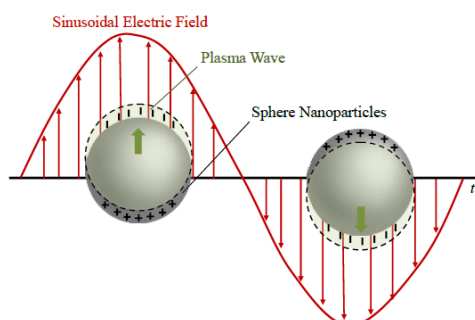

Figure 2. Schematic diagram of the LSPR effect.

For metal NPs with a radius much smaller than the wavelength of the incident wave, the local plasmon properties can be described by quasi-static approximation [22]. Since the particle size is

much smaller than the wavelength, the phase of the sinusoidal electromagnetic field can be regarded as constant on the whole particle. The external electric field drives the collective vibration of free electrons in the metal NPs, which forms an electromagnetic dipole vibration with positive charges in the lattice. By solving the Laplace equation in spherical coordinates and combining it with the continuity boundary conditions of the electric field, the polarizability of the electromagnetic dipole can be derived as follows.

$$\alpha = 4\pi R^3 \frac{\varepsilon(\omega) - \varepsilon_m}{\varepsilon(\omega) + 2\varepsilon_m} \tag{1}$$

where R denotes the radius of the NP, and $\varepsilon(\omega)$ denotes the dielectric constant of the NP, which is a function related to the frequency of the incident light and is complex, i.e., $\varepsilon(\omega) = \varepsilon_r(\omega) + i\varepsilon_i(\omega)$. where ε_m denotes the dielectric constant of the surrounding uniformly isotropic medium.

From the polarizability expression (1), the resonance phenomenon occurs when the denominator is the smallest, that is $\mathrm{Re}[\varepsilon(\omega)] = -2\varepsilon_m$. Therefore, the excitation of the LSPR effect requires that the dielectric constant of the material must be a negative number. Generally, the dielectric constant of metal materials such as gold (Au), silver (Ag), copper (Cu), aluminum (Al), or graphene meets the above conditions. It is well recognized that the optical properties of Au and Ag are highly sensitive to their size, shape (i.e., nanoshells, nanorods, nanorings and nanostars), as well as the surrounding environment [23], while Al has material properties that enable strong plasmon resonances across most of the visible region of the spectrum and into the ultraviolet, and the LSPR effect of Al is remarkably sensitive to the presence of oxide within the metal [24].

The resonance of the electromagnetic dipole is the direct cause of the resonance of the absorption and scattering spectra of NPs. For NPs of any morphology, the efficiency of the resonance process can be described by the absorption cross-section σ_{abs} and scattering cross-section σ_{scat}: when the LSPR effect occurs, in addition to the significant local electric field enhancement that occurs around the NPs, the absorption and scattering effect of the NPs on the incident electromagnetic waves reach the strongest, that is, the extinction cross-section σ_{ext} reaches the maximum [21].

$$\sigma_{abs} = k\,\mathrm{Im}(\alpha) - \frac{k^4}{6\pi}|\alpha|^2 \tag{2}$$

$$\sigma_{scat} = \frac{k^4}{6\pi}|\alpha|^2 \tag{3}$$

$$\sigma_{ext} = \sigma_{abs} + \sigma_{scat} = k\,\mathrm{Im}(\alpha) \tag{4}$$

where k is the wave vector of the incident light.

The electric field enhancement and the photothermal effect produced by the LSPR effect are important physical mechanisms for PNB generation and need to be introduced separately.

2.2. LSPR-induced electric field enhancement

The characteristic frequency of the LSPR effect is called the plasmon frequency. When the frequency of the incident radiation is close to or equal to the plasmon frequency, photons are greatly captured through the free electrons in the NP, resulting in an intensive electric field around the PNP surface [25]. As shown in Figure 3, the intensive electric field is always localized nearby the surface of PNP, and the relative intensity of the electric field always presents an exponential decay with the distance away from the PNP surface. The intensity and distribution of the electric field are closely related to the material of the PNP, the size and shape of the nanostructures, the dielectric properties of the surrounding environment and the wavelength and the polarization state of the incident laser radiation [18].

Unlike individual nanoparticle, the plasmonic dimer nanostructures shown in Figure 3e–f have tunable gap control, which creates a dramatic electromagnetic near-field confinement and enhancement in the nanogap, so-called "hot spots". In many recent reports, large near field enhancement has been demonstrated in metallic dimer nanostructures with various shapes like sphere, disk, rod, prism, and cube [26]. Similar to typical plasmonic dimer nanostructure, Figure 3g shows a schematic representation of a nanoparticle-on-metallic-mirror (NPoM) structure, in which a nanoparticle is separated from an underlying metal film molecular monolayer. The NPoM structure is more reliably and robustly fabricated [27]. Devaraj et al. [28] numerically investigated the influence of dielectric layer thickness on the plasmonic properties of NPoM structure. After that, they numerically compared the NPoM and free space dimer designs and studied their near-field enhancement characteristics to identify the similarities and differences between those two designs [29]. In addition, Chikkaraddy et al. [27] experimentally and theoretically compared the near-field and far-field optics of film-coupled nanocubes (termed nanocube-on-mirror, or NCoM) and nanospheres (nanoparticle-on-mirror, NPoM). The results of the above study indicate that the optical properties of NPoM are sensitive to the dielectric layer thickness, the nanoparticle shape and size, and the distance between nanoparticle and metal film.

Notably, the intensity of the local electric field is always far larger than the incident electric field and can even obtain tens of thousand times of the incident field. Such an electric field enhancement can be utilized in many applications that require high-intensity electric fields and nonlinear interactions with materials, such as surface-enhanced Raman scattering (SERS) [30], ultrafast laser cell nanosurgery [31], etc. In particular, gold nanostars (AuNSs), as shown in Figure 3d, have multiple sharp branches, creating the "lightning rod" effect that enhances the LSPR effect dramatically [32]. Based on the advantages of AuNSs including a tunable NIR plasmonic band, large surface area to volume ratio and strong LSPR enhancements at branches [33], their applications have been numerous in the biomedical field, including imaging [34], drug delivery [35,36] and photothermal therapy [37].
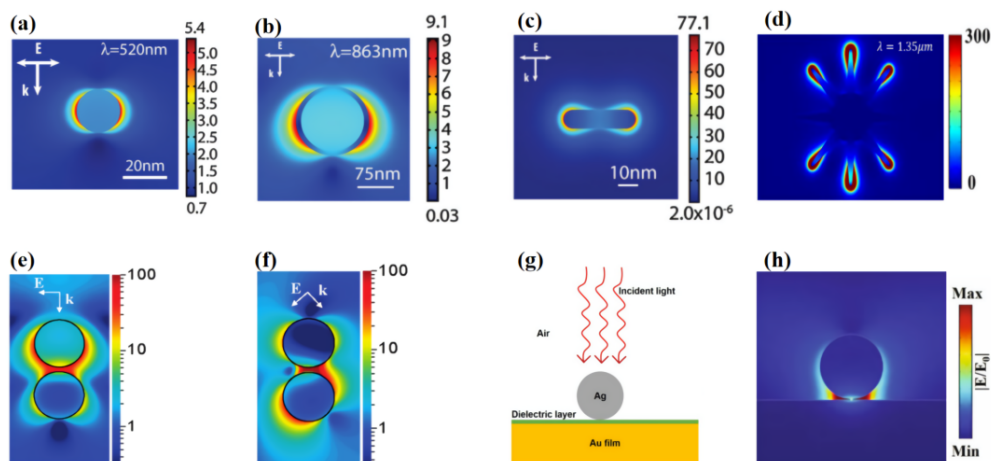
Figure 3. Local electric field distribution around different nanostructures under different incident radiation. (a) Electric field enhancement distribution around an AuNP with a radius of 25 nm irradiated at its LSPR effect wavelength of 520 nm [18]; (b) Electric field enhancement distribution around a 75 nm outer radius/65 nm inner radius SiO_2/Au nanoshell in water irradiated at LSPR wavelength of 863 nm [18]. (c) Electric field enhancement around a 10 nm × 41 nm Au nanorod in water irradiated along its long axis [38]. (d) Electric field enhancement distribution around an Au nanostar nanoparticle at 1350 nm resonance wavelength [39]. (e–f) Electric field enhancement distribution of Au dimer under different directions of incident radiation [21]. (g) Schematic representation of a nanoparticle on a metallic mirror separated by a thin dielectric layer [28]. (h) Electric field profiles taken for NPoM designs [28]. (E is the light polarization direction, k is the light transmission direction).

2.3. LSPR-induced photothermal effect

In addition to the local electric field enhancement, the LSPR effect induces the photothermal effect simultaneously. When the free electrons inside the PNP oscillate collectively in the presence of electromagnetic waves and collide with the lattice of the PNP, the energy is converted into heat, which is the physical mechanism of the LSPR-induced photothermal effect. Recently, the LSPR-induced photothermal effect and the consequent thermophysical response of metallic NPs induced by incident radiation have attracted great interest. Under the irradiation of a light source at a plasmon resonance frequency, PNPs can act as an efficient and highly localized heat source. More importantly, it can be remotely and flexibly controlled by the light source at the nanoscale. Depending on the light power, the NP geometry and the dielectric properties of the surrounding medium, the most direct effect of the photothermal effect of metallic NPs is the temperature increase in the NP and its surrounding medium [40]. If proteins are near metallic NPs, the proteins will be denatured due to the photothermal effect. Therefore, photothermal therapy can be used to kill cancer cells by increasing the local temperature of AuNPs under laser irradiation beyond the tolerance range of cancer cells [41]. If NPs are in an aqueous solution, laser heating will vaporize the water around the NPs to form PNBs [42], which can also be used to kill tumor cells [43]. Figure 4 shows the

thermophysical response of AuNPs as a function of temperature [44]. Owing to these excellent thermal effects, PNPs have shown increasing potential for applications in biomedical diagnostics [45], cancer therapy [46], microfluidic control [47,48] and other fields.
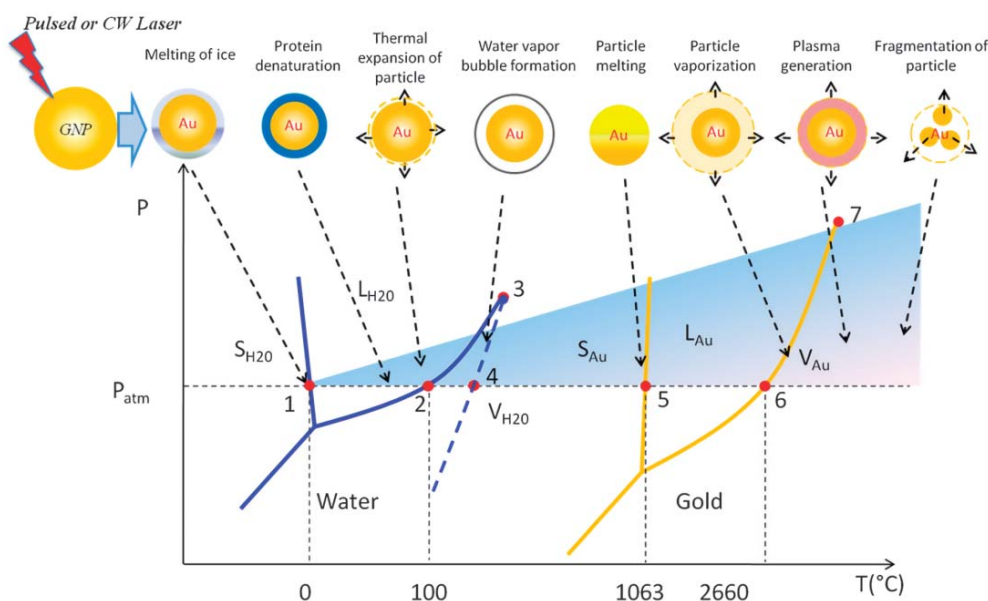

Figure 4. Schematic for thermophysical responses of laser AuNP heating including the phase diagrams. The top part shows that as the laser power increases from left to right, the particle surface temperature increases and leads to different thermophysical responses. The bottom phase diagram schematic shows the equilibrium thermodynamic states with the solid lines and the spinodal curve of water (non-equilibrium) in the blue dashed line [44].

Under the incident light irradiation, the heat absorbed by metal NPs can be calculated from Eq. (5) [49].

$$q(r) = \frac{1}{2}\varepsilon_0 \omega \operatorname{Im}[\varepsilon(\omega)]|E(r)|^2 \tag{5}$$

where ε_0 is the permittivity of vacuum; ω is the angular frequency of light radiation, $\varepsilon(\omega)$ is the relative permittivity of metal NPs, and $E(r)$ is the local electric field intensity, which can be obtained by numerically solving Maxwell's equations, shown in Eq (6), by numerical methods such as finite element modeling (FEM) or finite difference time-domain (FDTD) methods.

It can be found that the loss properties of metal NPs are directly reflected in the non-zero imaginary part of the metal material. The higher the electric field intensity, the more heat is absorbed by the NPs.

$$\nabla \times \mu_r^{-1}[\nabla \times E(r)] - k_0^2 \left(\varepsilon_r - j\frac{\sigma}{\omega \varepsilon_0}\right)E(r) = 0 \tag{6}$$

where μ_r, ε_r, σ denote the relative magnetic permeability, dielectric constant and electrical conductivity, respectively.
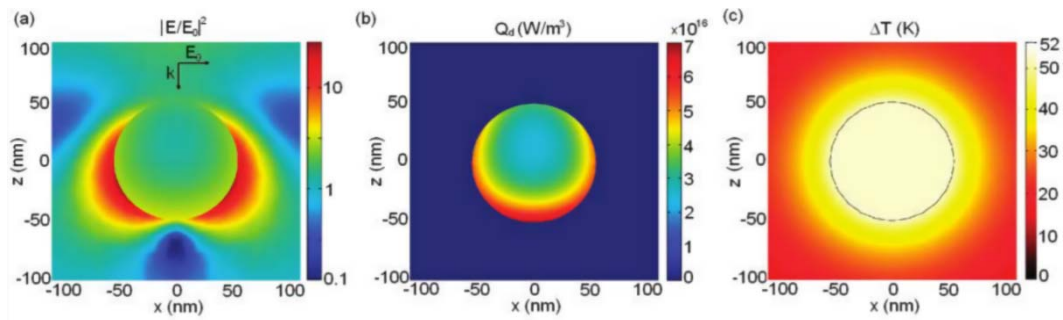
Figure 5. (a) Electric field distribution, (b) thermal power distribution and (c) steady-state temperature distribution of single AuNP with LSPR resonance laser irradiation [50].

Figure 5a shows the electric field distribution inside and outside of a single AuNP with a radius of 50 nm with planar light irradiation that undergoes the LSPR effect calculated by the FEM. Figure 5b shows the spatial distribution of the thermal power $q(r)$ derived using Eq (5). The incident light intensity in the calculation is 1 mW/μm² and the AuNP is assumed to be in transparent loss-free water with a refractive index of 1.33. Therefore, the thermal power is zero in water and the thermal power inside the particles is also non-uniformly distributed.

The total power P of the metal NPs can be obtained by integrating $q(r)$ over the whole particle, i.e., $P = \int_V q(r)dV$. The total power P comes directly from the absorption of the incident laser by NPs, namely:

$$P = \sigma_{abs}I_0 \tag{7}$$

where I_0 is the intensity of the incident laser (power per unit area).

In the absence of phase transformations and without considering thermal convection in the system, the heat transport can be described by the thermal diffusion equation as shown in Eq (8),

$$\rho(r)c(r)\frac{\partial T(r,t)}{\partial t} = \nabla \cdot \left[\kappa(r)\nabla T(r,t)\right] + q(r,t) \tag{8}$$

where $T(r,t)$ is the temperature as a function of the coordinates r and time t. $\rho(r)$, $c(r)$, $\kappa(r)$ are density, specific heat and thermal conductivity, respectively.

The thermal response of different nanostructures such as spheres, disks, core-shell structures, rods and cages has been extensively studied [44]. However, simple nanostructures are no longer sufficient for various applications based on the LSPR-induced photothermal effect. Therefore, there is an urgent need to explore nanostructures with higher photothermal temperatures and methods for their synthesis, as well as means for accurate measurements of the local temperature near the nanostructures. Toroghi et al. [51] analytically and numerically investigated the optical response of heterogeneous plasmonic trimer structures consisting of a silver nanoparticle dimer and a central gold nanoparticle to maximize the attainable temperature change for a given optical irradiance. Using a newly developed far-field thermal microscopy technique based on the temperature-dependent photoluminescence lifetime of thin-film thermographic phosphors, Coppens et al. [6] experimentally characterize the thermal response of various antennas and superstructure designs. Kulkarni et al. [52]

presented multiconcentric nanoshells with small size and high tunability and conducted a first-principles investigation of the optical properties of this structure.

3. Plasmonic nanobubbles: birth, growth and development

The study of the mechanism of PNB nucleation and development is of great significance for the research of PNB-based applications: it not only provides the theoretical basis and optimized implementation parameters for the relevant applications, but also makes the manipulation methods of various PNB-based applications more precise and flexible. Under the effect of incident radiation that excites the LSPR effect, there are two mechanisms of PNB nucleation: thermo- and plasma-mediated mechanisms [7]. The former is due to the heated PNPs dissipating their energy to the surrounding environment by thermal diffusion to provide energy for PNB formation. Recent studies on the mechanism of themo-mediated PNB nucleation have focused on the temperature of PNB nucleation [53]. However, the plasma-mediated PNB nucleation mechanism is different from the former: the local electric field enhancement accompanying the LSPR effect directly causes the transformation of liquid molecules into gaseous state due to the violent motion. In fact, both nucleation mechanisms are likely to coexist in the nucleation and development process of PNB, but for different materials of PNPs or different radiation source conditions, each of these two mechanisms has a different bias on PNB formation.

3.1. Thermo-mediated PNB nucleation

As shown in Figure 6, superheat is likely to occur around PNPs with incident radiation. Superheat characterizes the fluid state that remains liquid state above the boiling temperature. Hühn et al. [54] studied the generation of PNBs around AuNPs under CW heating and assumed a superheat of the surrounding medium. It was shown that the temperature around AuNPs on the glass substrate was up to 230 °C [55]. This temperature limit can even reach 300 °C if water is degassed. At this point, the heat source is no longer connected to the liquid water, which greatly reduces the heat dissipation, and the temperature peak inside the PNBs exceeds 700 °C [56].

The production of PNBs requires reaching the nucleation temperature, and whether and when the initial bubble nucleates depends on the competition between the laser heating and cooling due to thermal diffusion. Although we are accustomed to the formation of the bubbles at the boiling point of water, i.e., 100 °C, which is not the case for PNB nucleation. In most PNFs, the samples are so clean that bubbles cannot form at relatively low temperatures due to the absence of nucleation centers. Instead, there is an upper limit for the bubble formation temperature, which is about the spinodal temperature of 280 °C, assuming the system is at standard atmospheric pressure. At this temperature, water vapor and liquid water are indistinguishable, and exceeding this temperature, only water vapor exists. The formation of PNBs can be observed between boiling temperature and spinodal temperature due to the random density fluctuation within the PNF. However, the presence of impurities and gases decreases the nucleation temperature, and the nucleation temperature is independent of the laser power [57].
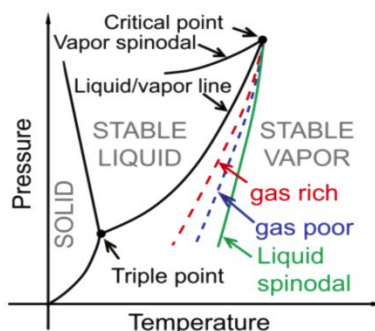
Figure 6. Phase diagram of water (schematics). The green solid line is the liquid spinodal line, which is the theoretical limit of superheat, while the blue and red dashed lines schematically depict the attainable superheat for gas-poor and gas-rich water, respectively [57].

In 2013, Fang et al. [53] combined dark-field scattering measurements based on LSPR shifts with surface-enhanced Raman scattering (SERS)-based temperature measurements on individual AuNP to investigate plasmon-induced PNB from an individual AuNP deposited on a substrate. The combination of local optical measurements at an individual AuNP can determine several key microscopic parameters of the system, such as the PNB radius around the NP surface, the internal PNB pressure, the NP surface temperature and their dependence on the incident light intensity. The results show that the vapor shell thickness around an individual AuNP with a radius of 50 nm is 6.5 nm with the intensity of the incident laser of 25 mW. The calculated vapor temperature inside the PNB is 464 K and the corresponding internal pressure is 1.49 MPa.
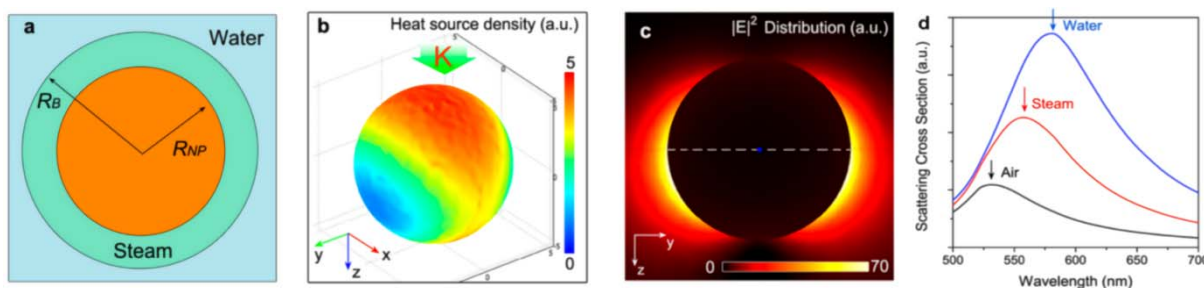

Figure 7. PNB theoretical modeling. (a) Schematic of PNB formation around an individual NP under 532 nm laser illumination. (b) Simulated heat-source density for an illuminated 100 nm diameter AuNP immersed in water. Light is incident along the z-axis and linearly polarized along y. (c) Near-field intensity enhancement for a 100 nm diameter AuNP in water. (d) Mie calculation of the scattering cross sections for a 100 nm diameter AuNP in the air (black), surrounded by a steam bubble with outer radium $R_B = 60$ nm (red), and in water (blue) [53].

In 2014, Baffou et al. [55] directly observed the temperature of PNB nucleation by temperature imaging using quadriwave shearing interferometry (TIQSI). In this study, a regular array of closely packed AuNPs was irradiated with a focused laser, and the diameter of the focal point varied

between 4.6–64 μm. As shown in Figure 8, the results show that the PNB nucleation occurs at about 220 °C in all cases.
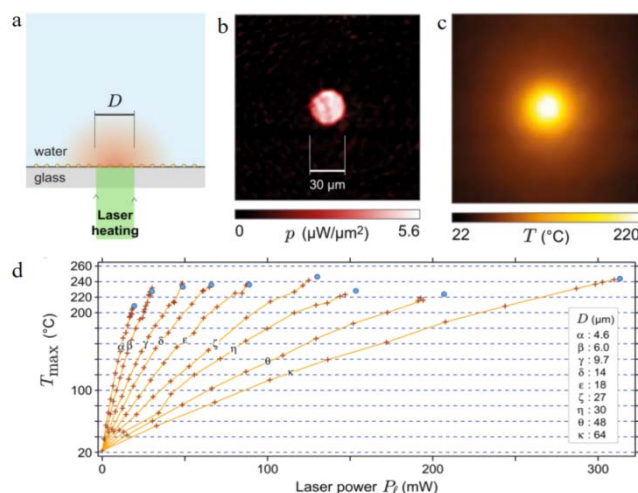

Figure 8. (a) Schematic of the experiment. (b) Heat source density. (c) Temperature map retrieved from image c, featuring a maximum temperature of 220 °C. (d) Maximum temperature T_{max} as a function of the laser power P_l for a set of various beam diameters D [55].

In 2017, Alaulamie et al. [56] introduced a sensitive method for measuring the local temperature using erbium oxide nanoparticle clusters, which was used to probe the temperature of PNB nucleation in degassed and nondegassed water. The results show that the average nucleation temperature for degassed water is 560 K, but this temperature is lowered by 100 K when gas is introduced into the water.

3.2. plasma-mediated PNB nucleation

The above measurements of PNB nucleation temperature are based on the themo-mediated mechanism of PNB nucleation theory. However, Lachaine et al. [58] proposed a plasma-mediated mechanism of PNB nucleation in the case of femtosecond pulses irradiation. To our knowledge, this work may be the first clear report for plasma-mediated PNB nucleation. As shown in Figure 9, the size of the laser-induced PNB depends on the polarization of the incident PL when the pulse duration is reduced to less than 1 ps. The difference between the PNB sizes produced by linearly and circularly polarized PL indicates that polarization-dependent PNB nucleation is a clear sign of the plasma-mediated mechanism. For long pulses, PNB nucleation is due to the laser energy absorption in AuNPs, followed by conductive transfer at the water interface, as shown in Figure 9a. For shorter pulses, the PNB nucleation is plasma-mediated. This difference is due to the nonlinear interaction of the enhanced field with the water molecules directly in the near-field, creating a localized photoexcited plasma that yields the PNB.
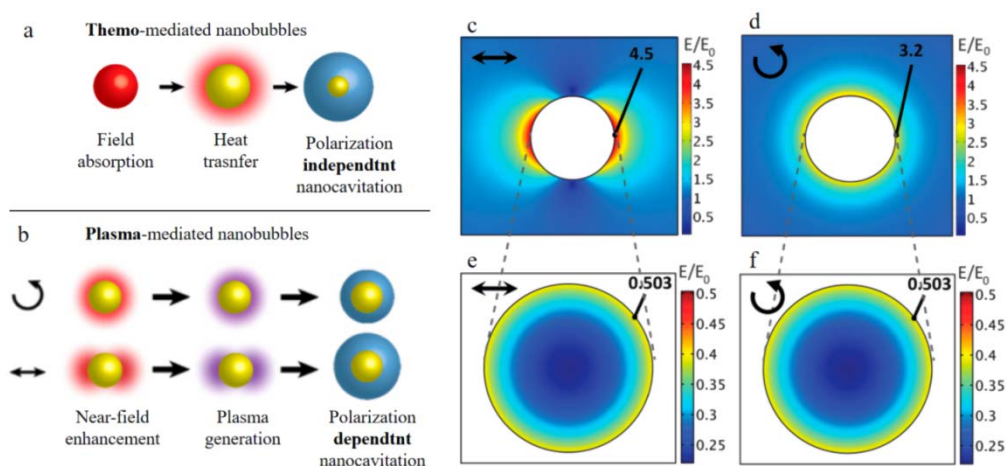
Figure 9. Schematic comparison of thermo-mediated and plasma-mediated PNB nucleation mechanisms. (a) Thermo-mediated PNB nucleation. (b) Plasma-mediated PNB nucleation. (c) Enhancement of a linearly polarized field is distributed at the poles of the 100 nm AuNP in water, and the maximum enhancement is 4.5. (d) Enhancement of a circularly polarized field is distributed all around the NP with a maximum of 3.2. (e) Absorbed field distribution inside the NP for linear polarization. (f) Absorbed field distribution inside the NP for circular polarization [58].

Recently, Shakeri-Zadeh et al. [7] schematically explained the possible processes of heat-mediated and plasma-mediated PNB generation (Figure 10). In the heat-mediated PNB generation process, when the AuNP is irradiated with radiation laser at a resonant frequency, its energy is first transferred to the free electrons of the AuNP, and the absorbed energy is transferred to the lattice of the AuNP through electron-phonon interactions, and each AuNP disperses its energy to its surroundings by thermal diffusion. During plasma-mediated PNB generation, the femtosecond pulsed radiation greatly enhances the electric field around the AuNPs, leading to nonlinear absorption of photon energy in the liquid, resulting in the generation the plasma. The rapid diffusion of the energy of the plasma causes a rapid increase in the pressure and temperature of the liquid, leading to PNB generation around the AuNPs.
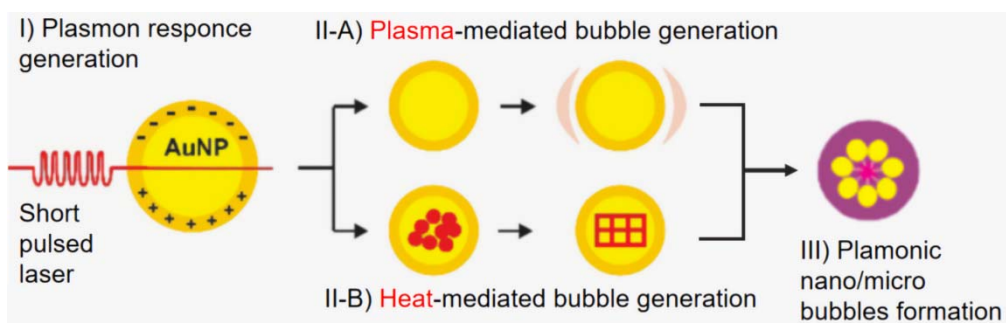

Figure 10. The processes possibly occur after the interaction of short PL with AuNPs. (I) interaction of short PL with AuNP and generation of surface plasmon, (II-A) plasma-mediated heating, (II-B) lattice transfer heating, (III) PNB formation [7].

However, Zhao et al. [59] showed that the plasma-mediated PNB process does not always occur only in the presence of short-pulse lasers, and silver nanofluid may also produce plasma-mediated PNBs under the irradiation of long waves. The strong effect of the local electric field oscillation on water molecules due to the LSPR effect was demonstrated by molecular dynamics (MD) simulations shown in Figure 11, and the reduction of the latent heat of vaporization of the nanofluid under the action of this electric field effect was calculated.
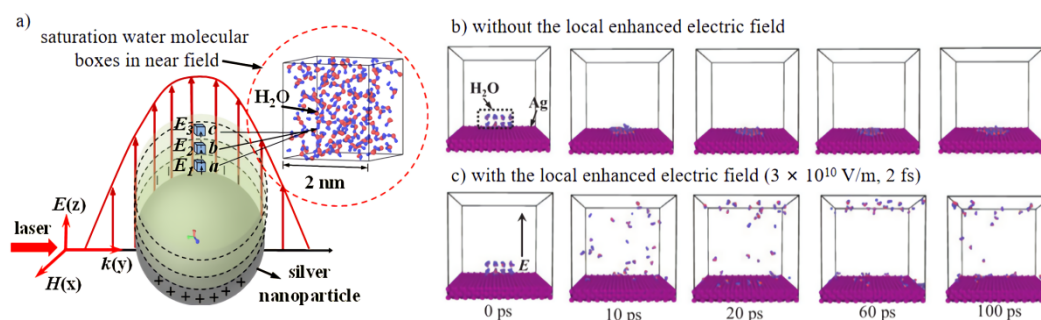
Figure 11. (a) MD simulation model. (b) The motions of water molecules on the surface of silver NPs in the absence of the local electric field. (c) in the presence of the local enhanced electric field with the intensity and period of 3.0×10^{10} V/m and fluctuation period 2 fs [59].

3.3. Growth and development of PNB

When the laser continues to illuminate PNF, the nucleated PNBs will continue to grow. However, the exact mechanism of PNB formation and growth has been widely debated. In particular, it is important to clearly determine the interaction between dissolved gas and water vapor in water during PNB growth, since the physical properties of vapor bubbles are quite different from those of gas bubbles. Specifically, the nature of vapor bubbles is controlled by the thermal diffusion, whereas gas bubbles are controlled by the mass diffusivity of the dissolved gas, which is about 100 times smaller than the thermal diffusivity [60].

In 2015, Liu et al. [61] generated PNBs on highly ordered plasmonic nanopillar arrays and observed a greater growth rate of PNBs in air-equilibrated water than in partially degassed water, highlighting the important role of dissolved gas in PNB formation. In 2017, Wang et al. [60] used ultrafast cameras to directly monitor the PNB growth in air-equilibrated and degassed water, respectively. A CW laser at a wavelength of 532 nm was used to irradiate the well-defined patterned AuNPs decorated surfaces in the experiment. The results are shown in Figure 12. For both air-equilibrium water and degassed water, the initial phase of PNB growth is controlled by the evaporation of water, and the growth kinetics of PNB are the same. After a transition time, the PNB growth is mainly caused by the influx of dissolved gas from the surrounding water. As a result, the PNB growth in degassed water essentially ceases, while the growth rate of PNB in air-equilibrium water increases at an appreciable rate. This work resolves the controversy regarding the role of dissolved gas and water vapor in PNB formation and provides important guidance for many PNB-based applications.
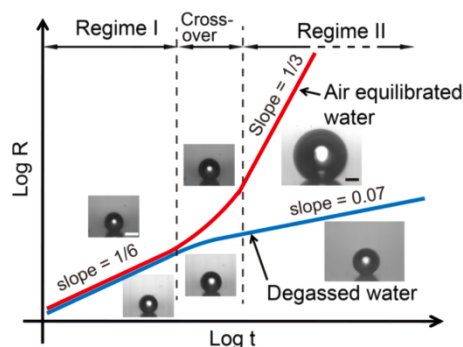
Figure 12. PNB growth process in air-equilibrated water and degassed water [60].

However, the above study did not quantify the role of dissolved gas in water in PNB growth. In 2019, Li et al. [62] quantified the effect of the amount of dissolved air on PNB nucleation and growth kinetics. As shown in Figure 13, the PNB nucleation temperature depends on the gas concentration: the higher the gas concentration, the lower the PNB nucleation temperature. In addition, the PNB growth, which is controlled by diffusion, is also controlled by the gas concentration. As Figure 13 shows, the maximum volume of the PNBs decreases with increasing gas concentration counterintuitively. This phenomenon can be explained by the increase in delay time τ_d, which decreases with increasing gas concentration, and the initial formation PNB is vapor bubble formed by water evaporation. Thus, a longer delay time leads to more energy dumped into the system, which results in a larger initial giant PNB [62].
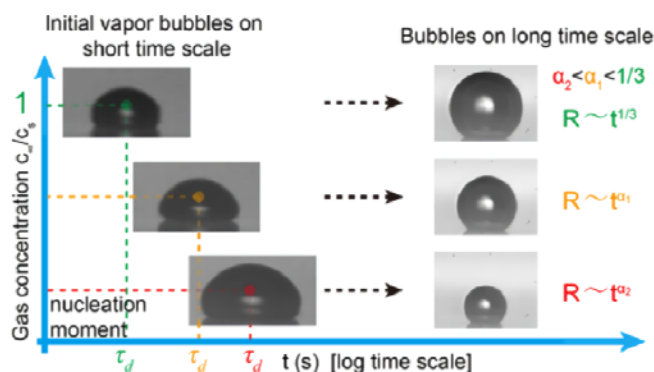

Figure 13. Initial giant bubble nucleation at different gas concentration levels. The PNBs nucleate after a delay (τ_d), which decreases with the increasing gas concentration [62].

In 2020, Zhang et al. [63] compared the growth dynamics of surface PNB generated in AuNPs suspensions and in deionized (DI) water with predeposited AuNPs on the surface with PL radiation. The results show that much faster PNB growth rates were observed in AuNPs suspensions compared with those in pure water with surface plasmonic structures. The volumetric heating effect around the surface PNBs due to the presence of AuNPs in the suspension is the key to explaining this difference. At the same laser power, volumetric heating increases the temperature around the surface PNBs more effectively than surface heating. In addition, the growth rates of the PNBs can be adjusted over a wide range by varying the concentration of AuNPs, the laser power and dissolved gas concentration.
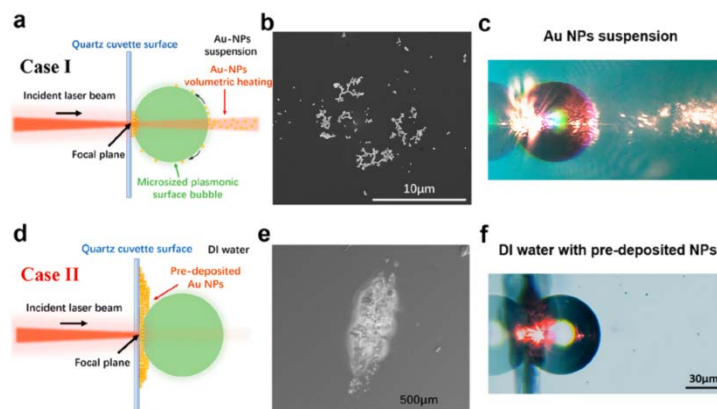
Figure 14. Schematic descriptions of microsized plasmonic surface PNB growth in (a) AuNPs suspension (case I) and (d) DI water with predeposited AuNPs on the surface (case II). Scanning electron microscope (SEM) images of predeposited AuNPs at the PNB nucleation site in (b) case I and (e) case II. Optical images from the side view of a surface PNB under laser illumination in (c) case I and (f) case II. The bright regions in (c) and (f) are from the laser scattered by predeposited or suspended AuNPs, respectively [63].

Once the heating laser stops, the PNB will shrink. For PNB consisting of a large amount of dissolved gas, the PNB shrinkage tends to be slow. The rate of shrinkage also depends on the size of the initial size of the PNB and usually takes several seconds to tens of minutes before fully disappearing [55]. This slow shrinkage is a result of the rate at which the gas can be reintroduced to the surrounding water. Therefore, the process is limited by the diffusion of gas within the water. As shown in Figure 15d, the PNB lifetime t scales with the radius as $t \propto r^{1/3}$. Interestingly, the growth of the PNB in air-equilibrated water has the same slope 1/3, shown in Figure 12, as in the case of PNB shrinkage.
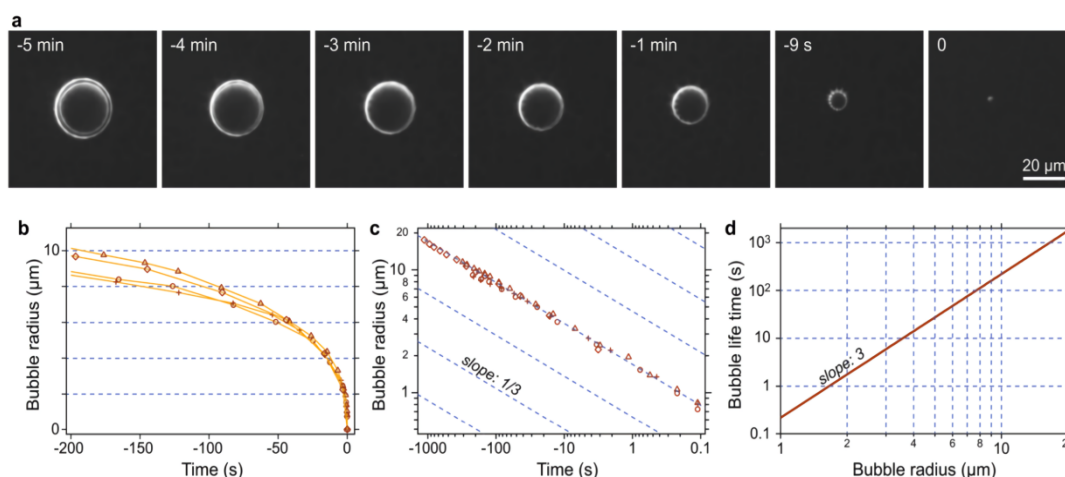

Figure 15. PNB shrinkage after heating laser turned off. (a) Dark field images of a PNB at successive times during shrinkage. (b) PNB radius as a function of time for four different PNBs. (c) Same date as image b but with log-log scaling. (d) PNB lifetime as a function of the initial bubble radius [55].

3.4. Marangoni convection caused by PNB.

When NPs are in an aqueous solution, PNBs will form around NPs with incident radiation. The temperature gradient along the gas-liquid interface leads to differences in surface tension along the surface, and when a part of the surface is heated, a Marangoni force from the hotter part to the colder part is generated on the surface and causes the fluid motion along the surface. This phenomenon is called the Marangoni effect or the thermocapillary effect [64].

Setoura et al. [64] described the formation of stationary PNBs and the subsequent Marangoni convection induced by CW laser heating of AuNPs in water. The results show that stationary PNBs with diameters of about 1–20 μm are produced by irradiating individual AuNP. The spatial distribution and velocity distribution of Marangoni convection around the PNBs can be observed by the wide-field fluorescence imaging of tracer nanospheres. To evaluate the PNBs-induced convection, numerical simulations were performed based on general heat diffusion equations and Navier-Stokes equations. Comparison between experimental and computational results shows that the temperature derivative of the surface tension on the PNB surface is a critical factor to control the Marangoni convection. The temperature difference of several Kelvin on the PNB surface leads to convective velocities in the range of 10^2 to 10^3 μm s^{-1}, which increases with increasing PNB diameter.
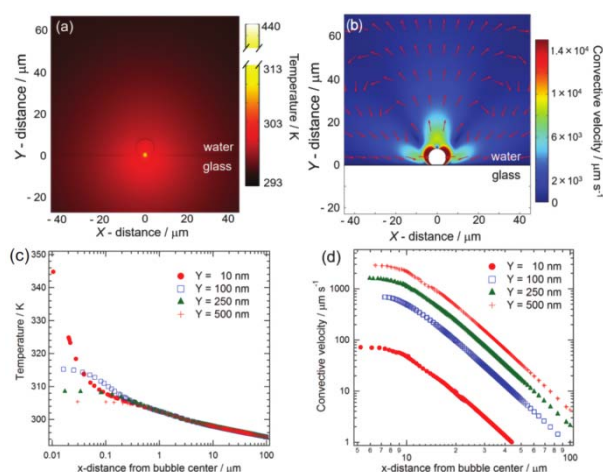

Figure 16. (a) Temperature distribution and (b) Velocity field of the system consisting of 8.6 μm diameter bubble, water, and glass substrate. (c) Temperature distribution along the x-axis at various y-distances obtained from (a). (d) Velocity profiles along the x-axis at various y-distances obtained from (b) [64].

Zhao et al. [65] simulated the temperature distribution and the Marangoni convection formed around the PNB. When the laser is focused on the gold-liquid interface (Figure 17a), the gold film at the laser focus is rapidly heated. As the water temperature near the laser focus reached its boiling point, a PNB is formed at the top of the gold film (Figure 17b). The simulation result of the temperature distribution around a PNB is shown in Figure 17c. The temperature decreases along the radial direction due to convection cooling along the top and bottom surfaces. The corresponding Marangoni convection caused by this temperature gradient is shown in Figure 17d. The convection flow creates a clockwise flow near the PNB-liquid interface due to the density difference caused by

the temperature difference in the water. The water flows toward the PNB near the bottom of the chamber, then moves upward to the top surface, and finally flows away. This convection plays an important role in attracting particles, which is an important step in the particle handling process [65].
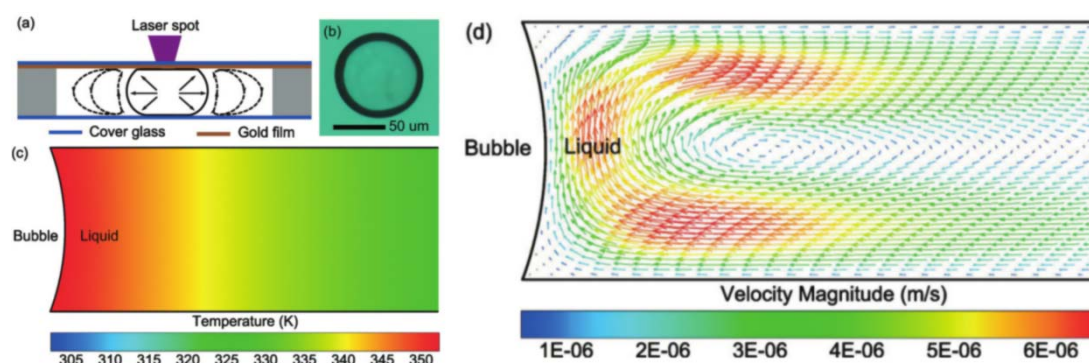

Figure 17. (a) Schematic of the PNB-generation process; (b) Microscope image of a PNB generated by the photothermal effect; (c) Simulation result of the temperature distribution around a PNB; (d) Simulation result of the convective velocity around a PNB [65].

In addition, this convection caused by the formation of PNBs has been reported to promote heat and mass transfer in continuous flow reactors for hydrogen production. Notably, the unique features of PNPs such as remarkable electric field amplification capability, extreme local heating, generation of high energy charge carriers and broad tunability of optical properties coupled with catalytically active surfaces provide exciting opportunities for hydrogen production with solar photochemistry. Compared to the typical non-plasmonic system, the hydrogen production rates of plasmonic system are approximately from one to even six orders of magnitude larger. This is due to the high quantum efficiency of plasmonic photocatalysts in converting photons into hydrogen [66].

3.5. Radiation-induced optical nonlinearity

Plasmonic nanofluids (PNFs) are characterized by significant optical nonlinearity at a rather low laser intensity (1 W cm^{-2}) and lead to a refractive index dependence of PNFs on the laser power [67]. The generation of PNB creates inhomogeneities in temperature, density and NP concentration in PNF, allowing various optical nonlinear effects such as the self-focusing effect [68], the thermal lens effect [69] and defocusing [70] have been observed in PNFs with laser irradiation.

When AuNPs are exposed to a focused laser with a plasmon frequency, the surrounding medium are heated due to heat dissipation of AuNPs, which produces a temperature gradient in the surrounding medium (Figure 18a). Since the refractive index of the fluid medium changes (usually decreases) with increasing temperature, a complex refractive index gradient forms spatially (Figure 18b–c).
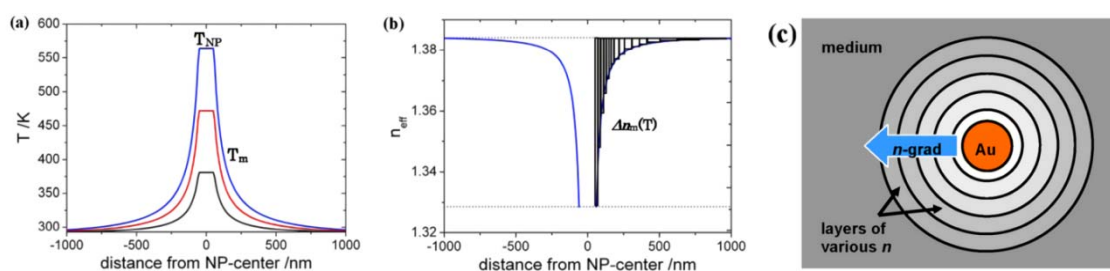
Figure 18. Schematic illustration of the temperature to refractive index profile transformation. (a) Temperature and (b) refractive index profiles of a 100 nm diameter point heat source. (c) A multi-layered core-shell model [71].

After the generation of the PNBs, the incident light will be reflected at the gas-liquid interface of the PNBs. Since the refractive index of the gas inside the PNB is smaller than that of the external fluid, the light injected into the bubble will be refracted, causing the scattering effect of the PNBs on the radiated energy. In addition, under the buoyancy and Marangoni force, PNBs will gradually rise and merge with the surrounding bubbles until they overflow the fluid surface and burst [72]. Thus, the existence of PNBs and their subsequent motion and merging have a great impact on optical nonlinearity.

Domínguez-Juárez et al. [73] used the apparatus shown in Figure 19 to study the thermal cycles that spontaneously commence when the incident laser grazed the meniscus of the PNF. The mechanism of the periodic heat cycle, based on the far-field images, is that the radiation energy is strongly absorbed and converted to heat and transferred to the surrounding liquid by the LSPR effect. Subsequently, the heated fluid expands and its refractive index decreases. Due to gravity, the hotter fluid rises, resulting in a higher refractive index below the light beam. As a result, the light refracts toward the colder fluid, resulting in instability and thus forming diffraction patterns on the rear screen. In addition, PNBs generated during the thermal cycle can facilitate this heat dissipation cycle.
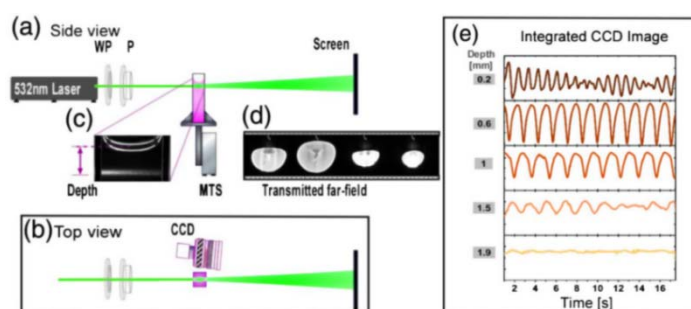

Figure 19. (a) Side and (b) top views of the experimental setup. The half-wave plate (WP) and polarizer (P) control the beam power and polarization (fixed horizontally), respectively, while the vertical translation stage (MTS) varies the entrance depth of light into the PNF. The CCD camera records the imaged beam pattern over time. (c) Side view of the cuvette with 80 nm AuNPs, which illustrates the propagation and depth of the light beam. (d) Four far-field patterns recorded during single oscillation cycle. (e) Plots of the integrated CCD images as a function of time for five different depths [73].

Besides, the clockwise Marangoni convection formed around the PNBs makes PNPs aggregate on the PNB surface [14]. With the merging and overflow of PNBs, PNPs will aggregate on the upper layer of the PNF, which leads to the non-uniform distribution of PNBs and PNPs in PNF, resulting in the non-uniform and non-linear radiation characteristics of PNF.

From the above analysis, it can be found that the temperature gradient generated by the PNPs will cause spatial inhomogeneity (refractive index gradient, etc.) of PNF and the motion and merging PNBs and the resulting aggregation of PNPs will cause temporal periodicity (periodic changes in refractive index, etc.) of PNF [74].

4. PBN-based applications

4.1. Active fluids manipulations

The most promising area for PNBs is as active control components in microfluidic systems. The presence of PNBs can physically prevent fluid flow, and it has been shown that the flow can be actively controlled by forming PNBs. As shown in Figure 20, Zhang et al. [12] used a CW laser to generate PNBs in microfluidic chips at any location in the microchannel. The effective generation of PNBs of controllable sizes can be achieved using a metal pad of different geometries immersed in various fluids.
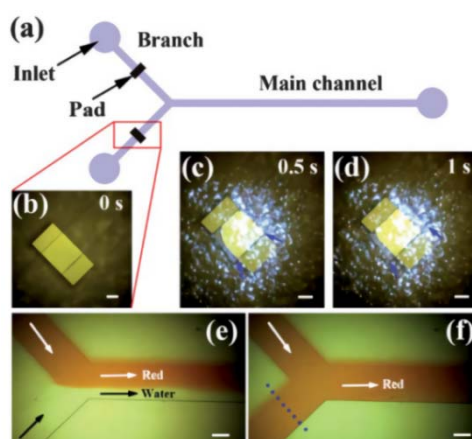

Figure 20. (a) A micro valve based on the laser-induced PNB in a Y-shaped microchannel. (b) Top view of the inlet channel where the PNBs are formed. (c) and (d) show the formation of the PNBs in the microchannel. (e) Open state of the valve, in which laminar flows with both red ink and water are visible in the main channel. (f) Closed state of the valve, in which the water inlet is blocked so that only the red ink flows in the main channel. Scale bar represents 200 mm [12].

Li et al. [75] demonstrated fast and reversible modulation of ion flow by a reversible plasma-controlled nanofluidic valve. The plasmonic nanopore can be used as a fluidic switch upon optical excitation. As schematically shown in Figure 21a, a laser with a wavelength of 785 nm was used to excite the LSPR effect of a plasmonic nanocavity integrated with a solid-state nanopore. A voltage was applied to measure the ionic current flowing through the nanopore. Figure 21b shows the

hysteresis behavior of the current change versus the laser power, which is mainly due to the formation of a PNB near the nanopore.
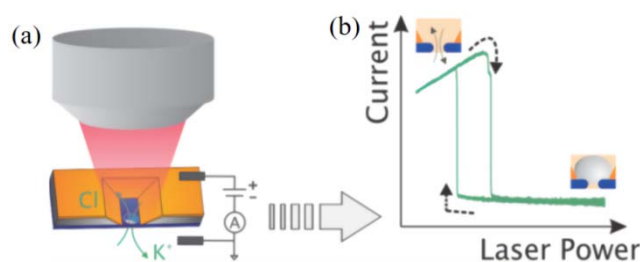

Figure 21. (a) Schematic of photoresistance switching of plasmonic nanopores. (b) Hysteretic behavior of the current change versus the laser power as a result of a PNB generation [75].

Unlike the direct obstruction of microchannels by PNBs to actively control the fluids, Liu et al. [48] presented a pioneering work to control fluid flow by using the plasmon-enhanced photothermal effect of AuNPs. As shown in Figure 22, AuNPs dispersed in fluids become localized heat sources upon radiation excitation and lead to fluid evaporation. The vapor condenses into droplets and coalesces with the original fluids, leading to a movement of the fluids. In the experiments, fluid flow in the microfluidic channels can be remotely guided at controlled speeds and directions using lasers with sub-milliwatt power.
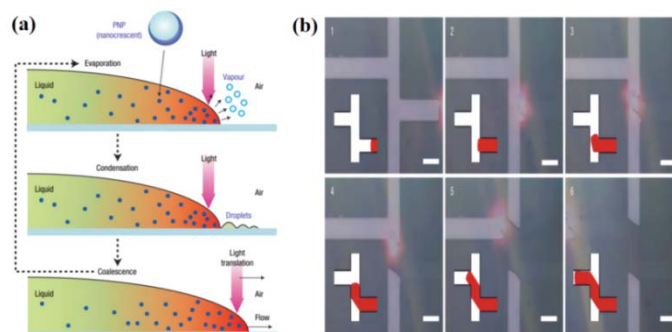

Figure 22. (a) Schematic diagram of the principle of the optically controlled fluid flow based on the plasmon-enhanced photothermal effects of AuNPs. (b) Continuous optical images show that the fluid flow can be optically guided into desired channels [48].

Additionally, active microfluidic manipulations have been achieved using PNBs-induced Marangoni flow generated by individual gold nanospheres [64] and gold nanoisland film (GNF) [13] under the incident radiation. By limiting the PNB diameter to approximately 10 μm, Namura et al. [13] achieved high flow rates close to 1 m/s, which is a powerful driving force for active fluid manipulations.

In 2015, Namura et al. [76] presented the control of Marangoni flow around a PNB using photothermal conversion. A focused laser was used as a highly localized heat source on

AuNPs/dielectric/Ag mirror thin films to generate PNBs and control the temperature gradient around the PNB at the micrometer scale. When the laser is irradiated next to the PNB, a strong main flow is generated and two symmetric rotation flows are developed on both sides of the PNB. Depending on the relative positions of the PNB and the laser spot, the shape of this rotation flow shows a significant transformation. Sorting of the polystyrene spheres (PS) with 0.75–2 μm diameters has been demonstrated using this controlled Marangoni flow.
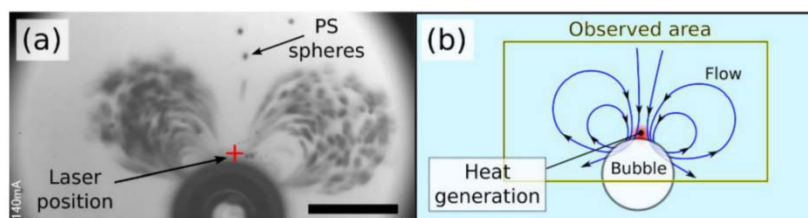

Figure 23. (a) Microscopic image of the rapid flow around the PNB induced by the photothermal conversion of AuNPs. The red cross shows the laser position, the small black dots are the PS spheres, and the large black circle indicates the PNB with a diameter of 65μm, respectively. Scale bar: 50 μm. (b) Sketch diagram of the flow around the PNB [76].

In 2016, Namura et al. [77] demonstrated the transition mode between the vertical and horizontal flow patterns of Marangoni flow around a PNB by using PS spheres with a diameter of 0.75 μm to visualize the flow. When the laser spot was located within a few micrometers from the center of the PNB, PS spheres dispersed in water were collected to the PNB underneath and ejected in one direction, forming a stable particles stream. The perpendicular temperature gradient helped collect the particles to the PNB underneath, while the horizontal temperature gradient contributed to the particles ejection. The high tunability of the PNB-induced Marangoni flow direction and origin is useful for developing advanced microfluidic systems.
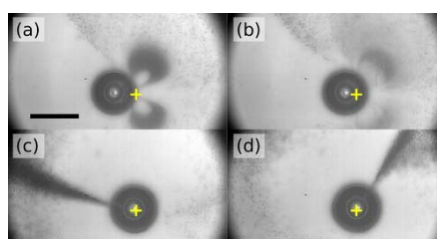

Figure 24. Series of microscope images showing the dependence of the thermo-plasmonic Marangoni flows around a PNB on the laser spot position. The small black dots are the PS spheres, and the big black circle are the PNB with a diameter of approximately 50 μm. The yellow crosses indicate laser spot positions. Scale bar: 50 μm [77].

In 2017, Namura et al. [13] studied the rapid Marangoni flows around a PNB using the LSPR effect of GNFs. By focusing a laser onto the GNF, a stable PNB with a diameter of about 10 μm was generated in degassed water, while a PNB with a diameter of larger than 40 μm was produced in

non-degassed water, and the maximum flow speed around the PNB was estimated to exceed 1 m/s. This rapid flow is attributed to the small PNB size and the superheat on the PNB surface in contact with the GNF.
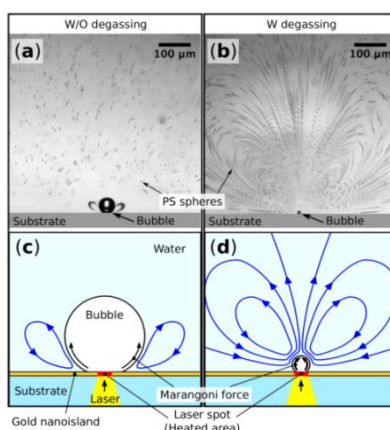

Figure 25. Observed flow around the PNB in water (a) without degassing and (b) with degassing. (c,d) show rough sketches of the flow directions in (a,b), respectively [13].

In addition to controlling the particles, Takeuchi et al. [72] described a noncontact method to manipulate PNBs using Marangoni flow based on the photothermal effect. As shown in Figure 26a,b, two kinds of Marangoni forces with different directions, F_{Mu} and F_{Md}, are present around the PNB. In addition, the buoyancy force F_b is also exerted on the PNB. Ultimately, the PNB position is determined by the balance between F_{Mu}, F_{Md} and F_b. As the laser power increases, the Marangoni forces become stronger and the buoyancy force can be relatively neglected, resulting in a downward shift of the balance position of the PNB. Therefore, the detachment of the PNB from the channel wall can be achieved by irradiating the heating laser in the vicinity of the PNB. The sequential images in the detachment are shown in Figure 26c. Specifically, the PNB detaches from the channel wall and approaches the laser point after detachment, and then the PNB stops its motion after reaching the laser point. Regardless of the initial PNB position, PNB detachment from the channel wall can be observed.
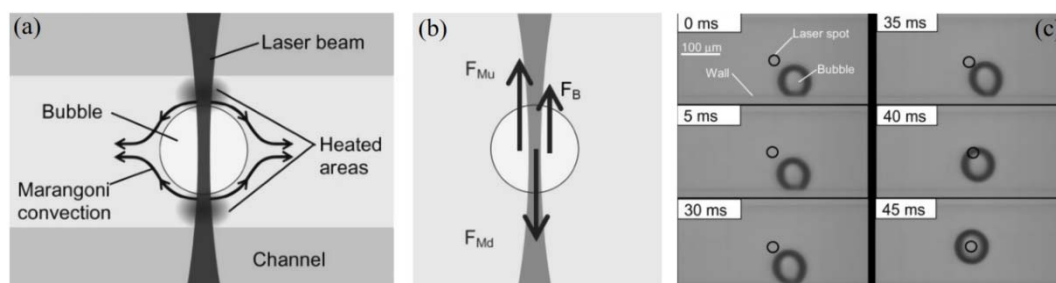

Figure 26. Schematic of suspending bubble balanced with Marangoni force and buoyancy: (a) Suspension model. (b) Forces exerted on a bubble. (c) Sequential images in detachment process of bubble from channel wall [72].

Yan et al. [78] demonstrated a new principle of bubble pulsating flow with top PL radiation on PNF with the device shown in Figure 27a, which is called microbubble piston engine. In addition, three states are identified based on pulse energy and laser frequency: regimes I, II, III refer to bulk circulation flow (BCF), laser-frequency-controlled bubble piston engine (L-BPE), and inertia-controlled bubble piston engine (I-BPE), as shown in Figure 27h.
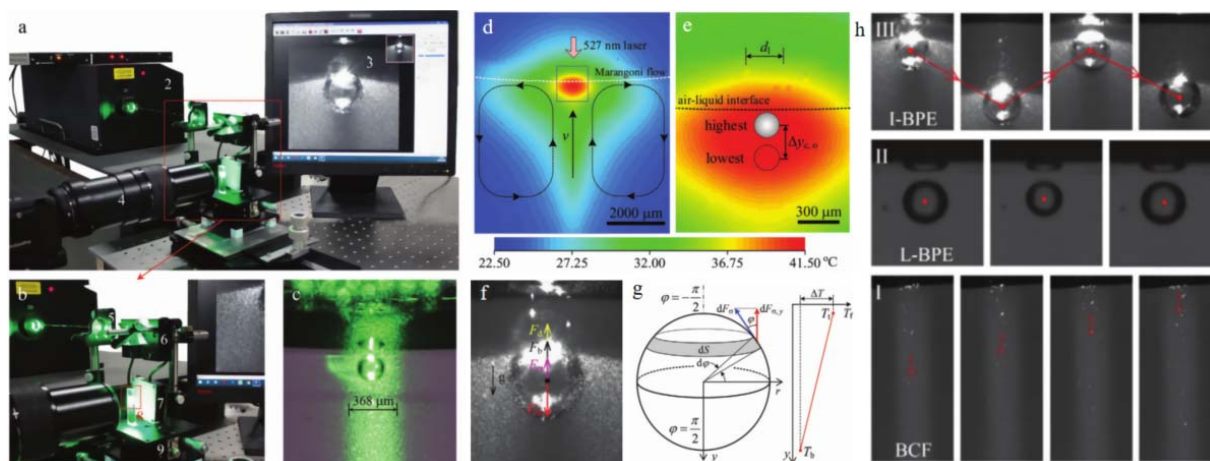

Figure 27. (a) 1, synchronizer; 2, 527 nm PL; 3, PC screen; and 4, high-speed camera. (b) 5, focusing lens; 6, reflecting prism; 7, back light; 8, cuvette containing nanofluid; 9, three-axis displacement platform. (c) Bubble observed due to photothermal heating. (d) Bulk circulation flow induced by temperature gradient on air-water interface. (e) hot spot region with the uniform temperature inside. (f) Forces analysis on PNB. (g) Marangoni force around a bubble. (h) The three regimes of laser-induced boiling in PNF [78].

In addition, the Marangoni convection induced by PNB can be used for particle manipulation. Fujii et al. [14] developed a new fabrication method for a ring structure of assembled NPs on an Au surface by using CW laser. As shown in Figure 28, the PNB formed on the AuNP surface by laser local heating acts as a template for the ring structure formation. Both Marangoni convection and capillary flow around the PNB are responsible for assembling NPs into the ring structure from PNF. Based on this method, various patterns of ring structures are easily performed by laser on/off operation without any templates. The resulting ring structure is strongly adsorbed on the gold surface and keeps its shape even by water washed or gently sonicated (at 40 kHz) treatment for 1 h.
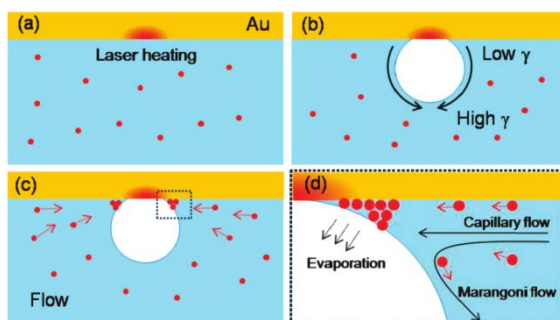
Figure 28. Schematic illustration of the mechanism of PNB formation and fluidic flow for assembling NPs (red dots). (a) The Au surface is heated by the focused laser beam in a PNF. (b) PNB formation. γ indicates the surface tension of water. (c) The surface tension gradient of the PNB interface is induced by a temperature gradient that produces a convective flow around the PNB to suck NPs toward the PNB. (d) NPs are agglomerated at the stagnation point made by the Marangoni flow and evaporation-induced capillary flow [14].

Li et al. [79] presented a microparticle aggregation technique *via* the optical fiber-excited LSPR effect of gold nanorods (AuNRs), depositing AuNRs on the designated surface of a tapered optical fiber (TOF). Through the enhanced photothermal effect, a PNB was formed on the TOF with a laser power of 14 mW. Marangoni convection transported AuNRs dispersed in water to the PNB, and strong optical gradient forces caused the particles to accumulate on the TOF surface. Figure 29a shows an optical image of the TOF decorated with AuNRs at a designated site indicated by the red dashed circle, and the inset shows a scanning electron microscopy (SEM) image of AuNRs (white spots) deposited on the TOF surface without aggregation. As shown in Figure 29b, when the PNB formed at a power of 14 mW, Marangoni convection squeezed AuNRs to the corners between the TOF surface and the PNB. As shown in Figure 29c, an accumulation of AuNRs was formed on the TOF surface.
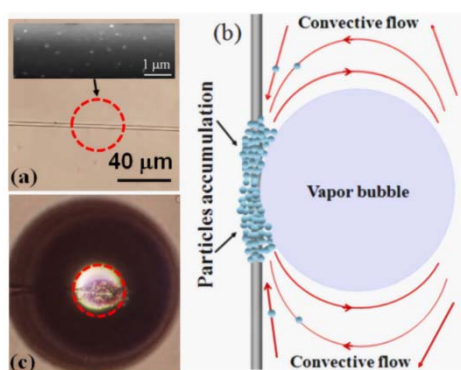

Figure 29. (a) Optical image of the TOF decorated with AuNR. (b) A sketch indicating Marangoni convection and movement of microparticles around the PNB. (c) Optical image showing microparticle aggregation on the targeted site of the TOF with the laser turned off [79].

Zheng et al. [80] used a low-power CW laser to generate PNBs by the LSPR effect obtained with a silver film. Microparticles dispersed in water flowed to the PNB due to the Marangoni convection and were accumulated on the silver film. The position of the PNBs can be easily controlled by moving the laser spot, as shown in Figure 30f–h, and micro-patterns can be written directly on the silver film with the accumulated microparticles.
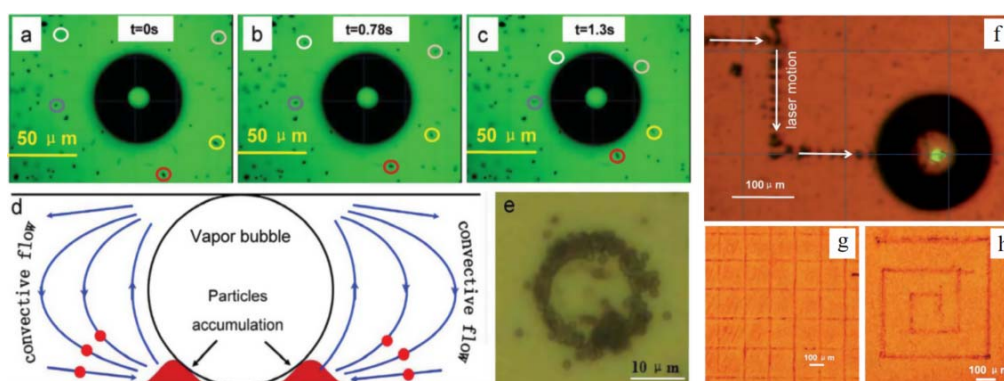

Figure 30. (a–c) The movement of microparticles near the PNB. (d) The Marangoni convection and movement of microparticles around the PNB. (e) A ring formed by accumulated microparticles around the PNB. (f) Microparticles accumulated along the route the PNB passes through. (g) Square lattice and (h) Swiss roll written by the microparticles [80].
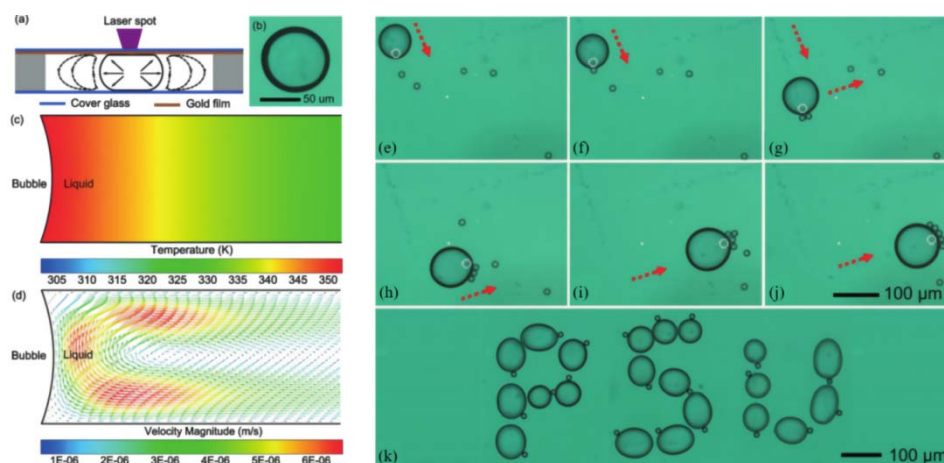
Figure 31. (a) Schematic of the PNB generation process. (b) Microscope image of a PNB generated by the photothermal effect. (c) Simulation result for the temperature distribution around a PNB. (d) Simulation result for the Marangoni convective flow pattern around a PNB. (e–j) Collecting randomly distributed polystyrene particles. (k) Single particle manipulation following three trajectories to trace the letters "P", "S", and "U" [65].

Zhao et al. [65] proposed a theoretical analysis and experimental demonstration of particle trapping and manipulation around the PNB. The results show that the drag force resulting from the

Marangoni convective can attract particles within 500 μm of a PNB surface. After the particle is in contact with the PNB surface, the balance between surface tension forces and pressure forces will trap the particles on the PNB surface, so that the particles move with the PNB without detaching. Using this approach, effectively collection of randomly distributed particles and manipulation of single particles along prescribed trajectories have experimentally demonstrated in Figure 31 e–k.

From the above analysis, it can be found that the process of PNB-based particle manipulation can be divided into the following three processes. First, the clockwise Marangoni convection caused by the temperature gradient around the PNB occurs. Then, once the particles are introduced into the convective flow field, the convection attracts the particles to the PNB surface. Finally, when the particles approach the PNB, they will be trapped on the PNB surface under the action of surface tension force and pressure force [65]. This technique is useful in many applications where high precision particle manipulation is required, but the key problem in manipulating Marangoni convection around the PNB is the difficulty in controlling the temperature gradient flexibly and precisely at the micrometer-length scale [76].

4.2. Optical property tuning

Utilizing unique properties of surface plasmon polaritons (SPPs) occurring at the interface of metals and dielectrics, plasmonic devices are capable of confining light in dimensions smaller than the Abbe diffraction limit and implementing extremely large field enhancement. Significant progress has been achieved in the field of plasmonics, ranging from super-resolution imaging [81] and energy harvesting [82] to ultra-sensitive biochemical detection [83] and optical metamaterials [84]. However, most traditional plasmonic devices are built on metals and dielectrics in a solid state that lacks tunability and reconfigurability. The PNB-based reconfigurable devices provide a much broader tuning range of SPPs. The optical response of the system is solved by flexibly adjusting the properties of the PNB in the far-field without the need for materials with nonlinear optical properties. The optical properties of optofluidic (that is, fusion of optics and microfluidics) devices can be readily changed by precisely manipulating the flow rate and liquid compositions at small spatial scales.

Zhao et al. [15] created a plasmonic lens in a microfluidic environment using laser-induced PNBs on a metal film. As shown in Figure 32, laser-induced PNB on metal films changes the local refractive index for SPPs that propagate along the top surface of the metal. By precisely manipulating the size and location of the PNBs, as well as the phase front of the incident SPPs, three functionalities, that is, divergence, collimation, and focusing of SPPs from the plasmofluidic lens can be achieved. The shape of the PNBs can be controlled through various means, considerably expanding the functionality of the plasmofluidic lens. In addition, the refractive index of the liquid solution can be conveniently changed by injecting different liquids and controlling flow rates, offering additional degrees of freedom in the design of plasmofluidic devices.
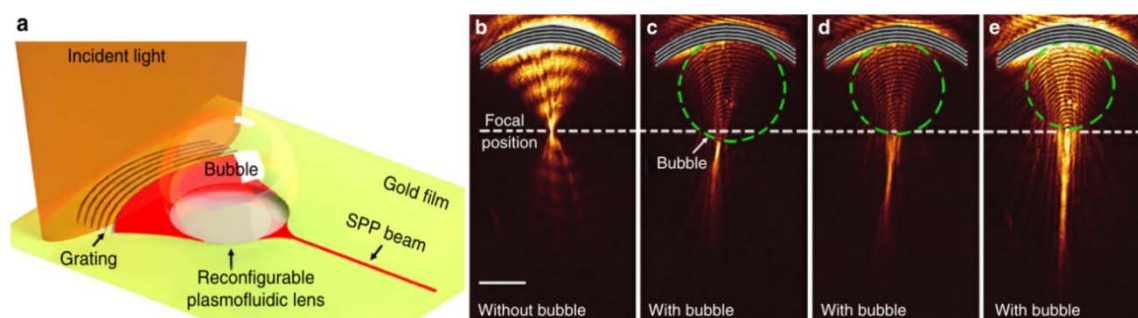
Figure 32. (a) Schematic of SPPs manipulation based on a PNB. (b) SPPs propagation without a PNB. (c–e) SPPs propagating through three PNBs with different diameters [15].

Compared to the modulation of SPPs with micro-sized PNBs, the generation of nano-sized PNB on plasmonic nanostructures allows for the control of light and heat at the nanoscale. Fang et al. [53] showed the change of the LSPR spectrum of an AuNP due to PNB formation. A CW laser was focused on an AuNP immobilized on a glass substrate in a liquid chamber as schematically shown in Figure 33a. The measured LSPR spectrum in the air was found to peak at 563 nm. When the microchamber was filled with deionized water with a temperature of 20 °C, the LSPR spectrum was observed to redshift to 598 nm. However, the LSPR was observed to blueshift to 581 nm during laser illumination when the NP was surrounded by water. The observed shift implies a decrease in the refractive index of the medium directly surrounding the NP, which is caused by the PNB formation surrounding the NP.
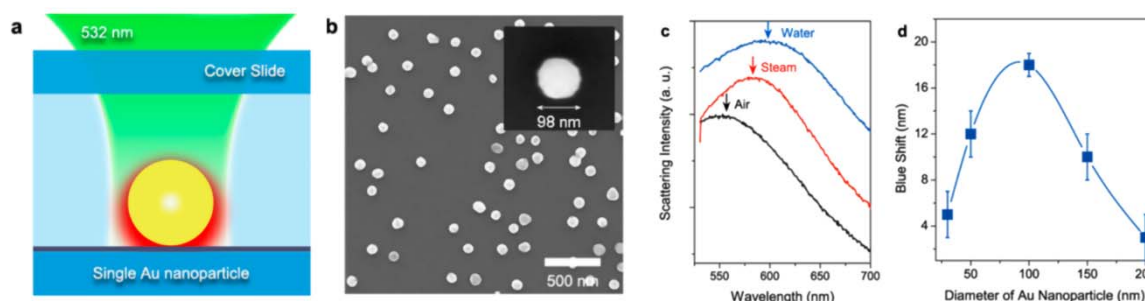

Figure 33. (a) Schematic of illumination and heating of a single AuNP by a laser beam. (b) SEM image of AuNPs on a glass substrate. (c) Scattering spectra of a 100 nm AuNP in air (black), water (blue), and an envelope of PNB (red). (d) Correlation between the PNB-induced peak shift in LSPRs of AuNPs and the particle diameter [53].

Recently, Gan et al. [85] demonstrated a wide-range tunable plasmonic device with high efficiencies by using the laser-induced PNBs in the metallic hole array structure. The water around the hole corners was heated by the laser, and the generated PNBs decreased the equivalent refractive index of the dielectric medium adjacent to the metal surface. Thus, the transmission spectrum of the hole array was blue-shifted. Experimentally, below the critical laser intensity, a wavelength shift of about 35 nm was observed. While above the critical laser intensity, a PNB that covered the whole hole array emerged, a refractive index change as large as 0.333 corresponding to a large wavelength

shift of about 200 nm was achieved. In addition, by controlling the size of the PNB, the transmission intensity could be tuned to cover the whole range from the peak intensity to the valley intensity of the metallic hole array. Such a large index variation can greatly reduce the design difficulty of tunable plasmonic devices; meanwhile increase the tunable range.
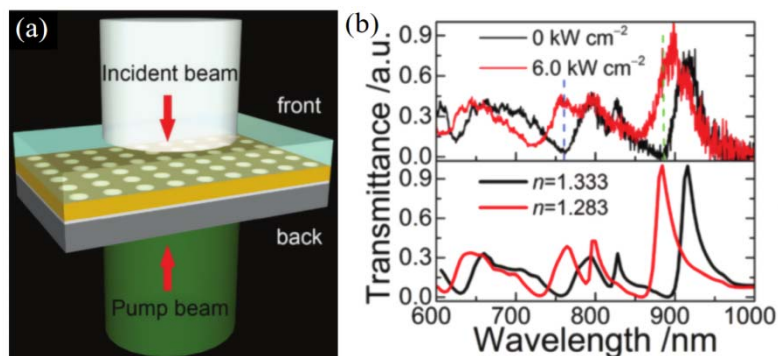

Figure 34. (a) Schematic of the all-optical tuning process in the hole array. (b) The top panel shows the measured zero-order transmission spectra with (red line) and without (black line) the PNB, and the bottom panel shows the corresponding simulation results [85].

4.3. Application in medical treatment

Biomedical demonstration of AuNPs has proven their biocompatibility, diagnostic and therapeutic possibilities [86]. Additionally, the size, mechanical properties and drug delivery characteristics of PNBs produced under the illumination of radiation laser can be flexibly tuned by controlling AuNPs properties and laser settings. In a biological environment, small-sized PNBs with shorter lifetimes are more suitable for precise disease imaging and diagnostic applications due to their excellent optical scattering properties [87]. While the medium-size PNBs with a longer lifetime are more favorable for drug delivery applications [88]. Finally, the largest size PNB with the longest lifetime is best suited for inducing mechanical cell damage and cancer cell destruction [7]. The unique optical and mechanical properties make PNBs a promising and valuable tool for biomedical applications.

4.3.1. Drug delivery

Accurate delivery of therapeutic and diagnostic agents is one of the greatest challenges in medicine. The drug concentration required to treat target cells is toxic to normal tissue, and the most advanced approaches to solve the agents delivery problem are based on their temporal encapsulation, delivery of the capsules to the target cells and controlled release from the capsule [89]. However, many of the release techniques (thermal, chemical and biological) can be harmful to healthy cells because they do not provide reliable protection of the capsule from the undesired accidental triggering of the release [43]. Furthermore, cellular defense mechanisms can make the intracellular delivery of therapeutic agents difficult. NPs, liposomes, and polymer-based and polyelectrolyte-based capsules, have been considered promising delivery vehicles because NPs are small enough to penetrate cells and can carry therapeutic agents and imaging probes, providing the

multiple functions of therapy and guidance. The main challenges of current delivery methods, however, remain to be the spatial and temporal control of the release and prevention of accidental premature release [90,91].

Anderson et al. [92] experimentally evaluated a new method of optically guided controlled release with liposomes containing molecular loadings and AuNPs. As shown in Figure 35, PL radiation was used to illuminate AuNPs to induce PNBs around the AuNPs to disrupt the liposome and eject its molecular contents. Thus, the release efficacy was tuned by varying the size and lifetime of the PNB and the PL power.
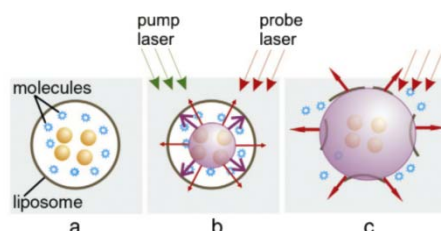

Figure 35. (a) Scheme of optically guided controlled release of encapsulated molecules with . (b) PNB disrupts the liposome and quickly ejects its content into outer medium. (c) Imaging and optical monitoring of the PNB [92].

Moreover, the PNBs open a new window to drug delivery into cells, as shown in Figure 36 [7]. PNB generates nanopores in the cell membrane to facilitate drug internalization into the target cells and overcome the dilemma of using large dose drugs due to poor cell penetration.
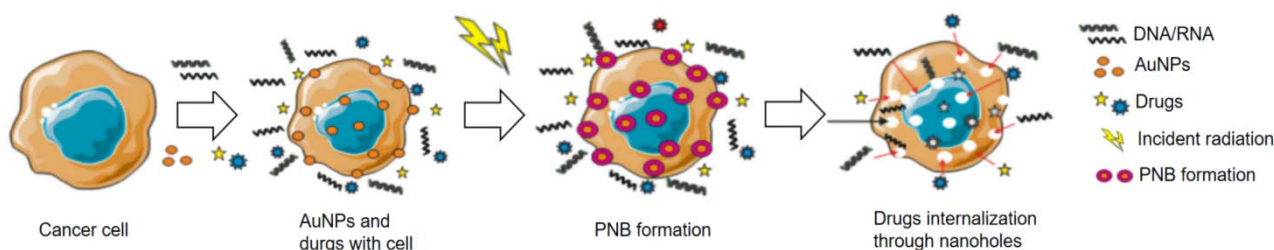
Figure 36. Mechanism of PNB-mediated drug delivery. Nanoholes are generated because of the formation of PNBs under the interaction of PL radiation, and the presence of nanoholes on cell membrane promotes the internalization of drugs [7].

4.3.2. Medical diagnosis and therapy

Photothermal therapy based on AuNP structures has been widely investigated as a state-of-the-art noninvasive therapeutic approach. Single NP cannot harvest sufficient energy, therefore, self-assemblies of small plasmonic particles into large aggregates are required for enhanced photothermal performance. Shao et al. [46] used self-assembled AuNRs in lipid bilayer-modified microcapsules to localize at tumor sites, generate PNBs under near-infrared light radiation, and subsequently damage tumor tissues. The resulting PNBs generated by microcapsules

achieve high efficiency of suppressing tumor growth compared to single AuNRs. In addition, the abilities of lipid bilayer-modified microcapsules to cross the biological barriers of the body and localize in target tissues have been demonstrated *in vivo* experiments. In addition, Huang et al. [93] demonstrated different mechanisms of cancer cells death. They designed a theranostic agent for novel cancer treatment by using an nanobubble-encapsulated hybrid nanosystem that can be monitored by ultrasound and fluorescent imaging and activated by near-infrared (NIR) light. The hybrid nanosystem comprised upconversion nanoparticle (UCNP) and mesoporous silica-coated gold nanorod (AuNR@mS) with the photosensitizer merocyanine 540 (MC540) to realize dual phototherapy. The theranostic agent was an AuNR@UCNP conjugate encapsulated inside a nanobubble. An energy of 808 nm NIR light passed from the UCNP to the AuNR, thereby conferring the AuNR a plasmonic effect with high temperature. Moreover, the plasmonic enhancement caused a synergistic effect on the MC540 photosensitizer to produce reactive oxygen species, thereby activating the apoptotic pathway of cancer cells. The results of *in vitro* and *in vivo* analyses confirmed the curative effect of improved dual phototherapy.
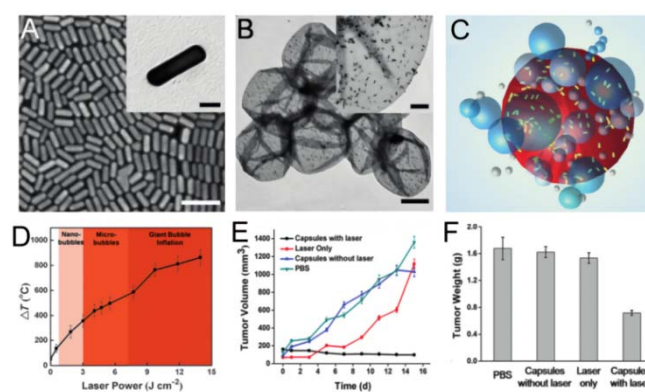

Figure 37. (A) SEM image of the GNRs. Scale bar: 100 nm. Inset: enlarged TEM image of a single GNR (scale bar: 20 nm). (B) TEM image of microcapsules (scale bar: 2 mm). Inset: higher-magnification TEM image of a single microcapsule (scale bar: 500 nm). (C) Illustration of PNB generation around GNR-capsules with near-infrared laser radiation. (D) Theoretical computation of the relationship between the increase of temperature and light power used. The colored regions correspond to different thermophysical responses. (E) Tumor growth curves of different groups of tumors after various treatments indicated. (F) Tumor weights after 15 days [46].

Cell theranostics is a new method that combines diagnostic, therapeutic and confirmation of therapy processes in a single process at the cell level, thereby improving both the rapidity and accuracy of diagnosis and therapy. The ideal therapeutic agent will support all the three abovementioned functions in *vivo*, allowing individual assessment of disease state and the eliminate diseased cells, while keeping healthy cells intact [94]. Different from the surface-enhanced Raman scattering and surface-enhanced fluorescence effects based on the LSPR effect of metal nanostructures, the radiation-induced small PNBs formed in cells have unique optical characteristics that can be detected by the probe laser, therefore, can be used for medical diagnosis; subsequently larger PNBs can mechanically destroy cancer cells without damaging the surrounding healthy tissues.

Rapid and sensitive diagnostics of infectious diseases is an urgent and unmet need as evidenced by the COVID-19 pandemic. Liu et al. [95] reported a novel strategy for single-particle digital assay based on digital plasmonic nanobubble detection (DIAMOND). PNBs are sensitive to the physical parameters of NPs such as sizes, shape, concentration, and clustering state. Taking advantage of these unique properties, an optofluidic setup was designed to flow the NP suspension in a micro-capillary, as shown in Figure 39. The focused laser beam probes a microscale "virtual compartment" and detects the PNB generation from single particles. When applied to detect respiratory syncytial virus, DIAMOND provided a 150-fold sensitivity enhancement over the state-of-the-art lateral flow assay and sample-to-answer time within 2 minutes.
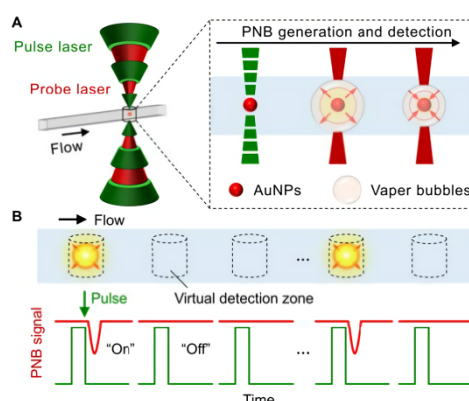

Figure 38. Schematics illustration of the DIAMOND concept. (A) Spectroscopy-based signal generation and detection. AuNPs are used for the generation of the PNBs by short laser pulses, which are subsequently detected by a secondary probe laser due to the optical scattering. (B) Detection principle based on optofluidic scanning of the sample flowing through. The "on" and "off" refers to the positive and negative PNB signals representing the presence or absence of targets.
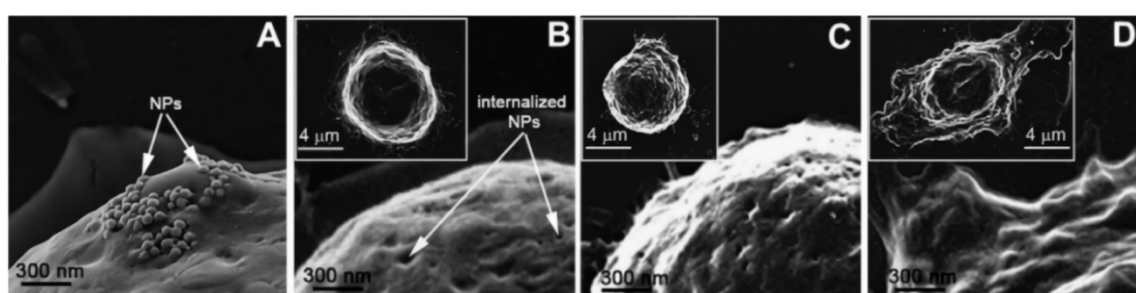
Figure 39. SEM images of cancer cells after the incubation with AuNPs show their (A) membrane coupling and (B) internalization. (C) Exposure to a PL laser. (D) The ablative PNB. The inserts show the images of the whole cells [96].

Wagner et al. [96] developed and evaluated PNBs as a tunable theranostic cellular agent in zebrafish hosting prostate cancer xenografts. In *vivo* experiment, PNBs were selectively generated around AuNPs in cancer cells with short PL. By dynamically varying the energy of the PL, an initial

small PNB detected the cancer cell through optical scattering, followed by a larger PNB that mechanically ablated the cancer cells without damaging the surrounding tissue, while its optical scattering confirmed the cell destruction.

5. Conclusions and perspectives

In this review, first, we summarize the mechanism regarding the generation of PNBs and PNB-based applications. The LSPR effect occurs in NPs induced by laser radiation at resonant wavelength, which causes a significant enhancement of the local electric field around the NPs and thus induces a photothermal conversion process that is essentially a Joule effect. When the NPs heat the surrounding medium to generate PNBs, Marangoni convection and optical nonlinearity are induced under the influence of temperature gradient.

Then, we summarize the nucleation mechanism and growth change of PNBs. The results indicate that the nucleation of PNB may be due to the combined effect of heat transfer and local enhanced electric field. During the PNB nucleation process, the PNB nucleation temperature, between the boiling point temperature and the spinodal temperature, shows an inverse relationship with the dissolved gas concentration in water. What is more, the growth of PNB in air-equilibrium water is initially controlled by the evaporation of water, and the subsequent growth and dissipation are mainly controlled by the diffusion of the dissolved gas in water.

Finally, we review PNB-based applications in active fluids manipulations, optical property tuning, and medical treatment. Since the properties of PNBs can be remote and flexible tuning by adjusting radiation parameters, it is possible to actively control the generation and location of PNBs and the Marangoni convection around the PNBs, thus providing active control of fluids and particles. Additionally, the refractive index of the medium can be flexibly adjusted by changing the PNF type and radiation parameters, which can be used for tunable plasmonic devices. In the biomedical field, the position, size and lifetime of PNBs can be precisely controlled by controlling the NP properties and radiation parameters. Specifically, small PNBs can be generated by low fluence radiation laser for non-invasive imaging and diagnostics, while increasing laser fluence will convert them into destructive agents for drug delivery and cancer cell destruction at the cell level. With the rapid development in the field of LSPR technology, there is no doubt that PNBs will provide amazing applications in microfluidic control, disease diagnosis and therapy, etc. Here, we provide some new insights into the future of this promising field.

1. Although the mechanism of thermo-mediated PNB nucleation has been widely accepted, the understanding of the mechanism of plasma-induced PNB nucleation is still insufficient. Specifically, there is still a lack of research on the conditions, limitations and quantitative parameters of the latter mechanism in different environments, and further investigation is also needed on the growth kinetics of PNB growth based on this mechanism.

2. The study of the optical nonlinearity in the PNB growth process is still relatively preliminary, and quantitative research on the spatial inhomogeneity and temporal periodicity of the resulting optical properties is needed.

3. In the PNB growth process, the optical characteristics of the fluid, especially the spectral characteristics and their effects on the heat transfer and micro-convection processes, still lack in-depth studies. For example, the aggregation of PNPs during the PNB growth process has a large effect on the resonance spectrum of LSPR. Meanwhile, the influences of the refraction and scattering

properties at the gas-liquid interface of PNBs on the PNB-based microfluidic manipulations are also worthy of in-depth research.

4. The interaction between PNBs and PNPs lacks a comprehensive study. In the existing works, the analysis of the interaction forces between PNBs and PNPs still lacks precise quantitative studies.

5. Based on the deeper understanding of the physical mechanism of PNB, the application-level technology is expanding in several emerging fields, and the accuracy requirements on the temporal and spatial scale of manipulation are gradually increasing. Meanwhile, in the field of microfluidic manipulation, more attention is paid to the development of new nanomaterials with low cost and high reliability or the exploration of new regulation techniques, while in the field of biomedical, practical issues such as biocompatibility are worthy of in-depth research.

Acknowledgments

Conflict of interest

The authors declare that there are no conflicts of interest related to this study.

Reference

1. Li J, Zhang Y, Ding S, et al. (2017) Core-Shell nanoparticle-enhanced raman spectroscopy. *Chem Rev* 117: 5002–5069.
2. Valenti M, Jonsson M, Biskos G, et al. (2016) Plasmonic nanoparticle-semiconductor composites for efficient solar water splitting. *J Mater Chem* 4: 17891–17912.
3. Baffou G, Quidant R, Girard C (2009) Heat generation in plasmonic nanostructures: Influence of morphology. *Appl Phys Lett* 94: 153109.
4. Kelly K, Coronado E, Zhao L, et al. (2003) The optical properties of metal nanoparticles: the influence of size, shape, and dielectric environment. *J Phys Chem B* 107: 668–677.
5. Baffou G, Quidant R, Javier G (2010) Nanoscale control of optical heating in complex plasmonic systems. *ACS Nano* 4: 709–716.
6. Coppens Z, Li W, Walker D, et al. (2013) Probing and controlling photothermal heat generation in plasmonic nanostructures. *Nano Lett* 13: 1023–1028.
7. Shakeri-Zadeh A, Zareyi H, Sheervalilou R, et al. (2020) Gold nanoparticle-mediated bubbles in cancer nanotechnology. *J Control Release* 330: 49–60.
8. Kotaidis V, Dahmen C, Plessen G, et al. (2006) Excitation of nanoscale vapor bubbles at the surface of gold nanoparticles in water. *J Chem Phys* 124: 184702.
9. Gouesbet G, Rozé C, Meunier-Guttin-Cluzel S (2000) Instabilities by local heating below an interface. *J Non-Equil Thermody* 25: 337–379.
10. Zwaan E, Gac S, Tsuji K, et al. (2007) Controlled cavitation in microfluidic systems. *Phys Rev Lett* 98: 254501.

11. Fujii S, Kobayashi K, Kanaizuka K, et al. (2010) Manipulation of single DNA using a micronanobubble formed by local laser heating on a Au-coated surface. *Chem Lett* 39: 92–93.

12. Zhang K, Jian A, Zhang X, et al. (2011) Laser-induced thermal bubbles for microfluidic applications. *Lab Chip* 11: 1389–1395.

13. Namura K, Nakajima K, Suzuki M (2017) Quasi-stokeslet induced by thermoplasmonic Marangoni effect around a water vapor microbubble. *Sci Rep* 7: 45776.

14. Fujii S, Kanaizuka K, Toyabe S, et al. (2011) Fabrication and placement of a ring structure of nanoparticles by a laser-induced micronanobubble on a gold surface. *Langmuir: ACS J Surf Colloids* 27: 8605–8610.

15. Zhao C, Liu Y, Zhao Y, et al. (2013) A reconfigurable plasmofluidic lens. *Nat Commun* 4: 2305–2305.

16. Wang Q, Zhu D, Liu X, et al. (2016) Microneedles with controlled bubble sizes and drug distributions for efficient transdermal drug delivery. *Sci Rep* 6: 38755.

17. Min K, Min H, Lee H, et al. (2015) pH-controlled gas-generating mineralized nanoparticles: a theranostic agent for ultrasound imaging and therapy of cancers. *ACS Nano* 9: 134–145.

18. Boulais É, Lachaîne R, Hatef A, et al. (2013) Plasmonics for pulsed-laser cell nanosurgery: Fundamentals and applications. *J Photoch Photobio C* 17: 26–49.

19. Prosperetti A (2017) Vapor bubbles. *Annu Rev Fluid Mech* 49: 221–248.

20. Liu J, He H, Xiao D, et al. (2018) Recent advances of plasmonic nanoparticles and their applications. *Materials* 11: 1833.

21. Baffou G, Quidant R (2013) Therm plasmonics: using metallic nanostructures as nano sources of heat. *Laser Photonics Rev* 7: 171–187.

22. Sancho-Parramon J (2009) Surface plasmon resonance broadening of metallic particles in the quasi-static approximation: a numerical study of size confinement and interparticle interaction effects. *Nanotechnology* 20: 235706.

23. Ni Y, Kan C, Gao Q, et al. (2016) Heat generation and stability of a plasmonic nanogold system. *J Phys D* 49: 055302.

24. Knight M, King N, Liu L, et al. (2014) Aluminum for plasmonics. *ACS Nano* 8: 834–840.

25. Chen M, He Y, Wang X, et al. (2018) Numerically investigating the optical properties of plasmonic metallic nanoparticles for effective solar absorption and heating. *Sol Energy* 161: 17–24.

26. Huang Y, Chen Y, Wang L, et al. (2018) Small morphology variations effects on plasmonic nanoparticle dimer hotspots. *J Mater Chem C* 6: 9607–9614.

27. Kongsuwan N, Demetriadou A, Horton M, et al. (2020) Plasmonic nanocavity modes: From near-field to far-field radiation. *Opt Lett* 7: 463–471.

28. Devaraj V, Lee J, Oh J (2018) Distinguishable plasmonic nanoparticle and gap mode properties in a silver nanoparticle on a gold film system using three-dimensional fdtd simulations. *Nanomaterials* 8: 582.

29. Devaraj V, Jeong N, Lee J, et al. (2019) Revealing plasmonic property similarities and differences between a nanoparticle on a metallic mirror and free space dimer nanoparticle. *J Korean Phys Soc* 75: 313–318.

30. Pilot R, Signorini R, Durante C, et al. (2019) A review on surface-enhanced Raman scattering. *Biosensors* 9: 1–99.

31. Boulais É, Lachaîne R, Meunier M (2012) Plasma mediated off-resonance plasmonic enhanced ultrafast laser-induced nanocavitation. *Nano Lett* 12: 4763–4769.

32. Khoury C, Vo-Dinh T (2008) Gold nanostars for surface-enhanced raman scattering: Synthesis, characterization and optimization. *J Phys Chem C Nanomater Interfaces* 112: 18849–18859.

33. Liu Y, Yuan H, Kersey F, et al. (2015) Plasmonic gold nanostars for multi-modality sensing and diagnostics. *Sensors* 15: 3706–3720.

34. Golmohammadi S, Etemadi M (2019) Analysis of plasmonic gold nanostar arrays with the optimum sers enhancement factor on the human skin tissue. *J Appl Spectrosc* 86: 925–933.

35. Tomitaka A, Arami H, Ahmadivand A, et al. (2020) Magneto-plasmonic nanostars for image-guided and NIR-triggered drug delivery. *Sci Rep* 10: 10115.

36. Rodrigues RL, Xie F, Porter A, et al. (2020) Geometry-induced protein reorientation on the spikes of plasmonic gold nanostars. *Nanoscale Adv* 2: 1144–1151.

37. Liu Y, Chongsathidkiet P, Crawford BM, et al. (2019) Plasmonic gold nanostar-mediated photothermal immunotherapy for brain tumor ablation and immunologic memory. *Immunotherapy* 11: 1293–1302.

38. Yu Y, Chang S, Lee A, et al. (1997) Gold nanorods: electrochemical synthesis and optical properties. *J Phys Chem B* 101: 6661–6664.

39. Chen M, Wang X, Hu Y, et al. (2020) Coupled plasmon resonances of Au thorn nanoparticles to enhance solar absorption performance. *J Quant Spectrosc Ra* 250: 107029.

40. Richardson H, Carlson M, Tandler P, et al. (2009) Experimental and theoretical studies of light-to-heat conversion and collective heating effects in metal nanoparticle solutions. *Nano Lett* 9: 1139–1146.

41. Huff T, Tong L, Zhao Y, et al. (2007) Hyperthermic effects of gold nanorods on tumor cells. *Nanomedicine* 2: 125–132.

42. Lukianova-Hleb E, Hu Y, Latterini L, et al. (2010) Plasmonic nanobubbles as transient vapor nanobubbles generated around plasmonic nanoparticles. *ACS Nano* 4: 2109–2123.

43. Lapotko D (2009) Plasmonic nanoparticle-generated photothermal bubbles and their biomedical applications. *Nanomedicine* 4: 813–845.

44. Qin Z, Bischof J (2012) Thermophysical and biological responses of gold nanoparticle laser heating. *Chem Soc Rev* 41: 1191–1217.

45. Lim W, Gao Z (2016) Plasmonic nanoparticles in biomedicine. *Nano Today* 11: 168–188.

46. Shao J, Xuan M, Dai L, et al. (2015) Near-Infrared-Activated nanocalorifiers in microcapsules: vapor bubble generation for in vivo enhanced cancer therapy. *Angew Chem* 54: 12782–12787.

47. Donner J, Baffou G, McCloskey D, et al. (2011) Plasmon-assisted optofluidics. *ACS Nano* 5: 5457–5462.

48. Liu G, Kim J, Lu Y, et al. (2006) Optofluidic control using photothermal nanoparticles. *Nat Mater* 5: 27–32.

49. Govorov A, Zhang W, Skeini T, et al. (2006) Gold nanoparticle ensembles as heaters and actuators: melting and collective plasmon resonances. *Nanoscale Res Lett* 1: 84–90.

50. Chen X, Chen Y, Yan M, et al. (2012) Nanosecond photothermal effects in plasmonic nanostructures. *ACS Nano* 6: 2550–2557.

51. Toroghi S, Kik P (2014) Photothermal response enhancement in heterogeneous plasmon-resonant nanoparticle trimers. *Phys Rev B* 90: 205414.

52. Kulkarni V, Prodan E, Nordlander P (2013) Quantum plasmonics: Optical properties of a nanomatryushka. *Nano Lett* 13: 5873–5879.

53. Fang Z, Zhen Y, Neumann O, et al. (2013) Evolution of light-induced vapor generation at a liquid-immersed metallic nanoparticle. *Nano Lett* 13: 1736–1742.

54. Hühn D, Govorov A, Gil P, et al. (2012) Photostimulated Au nanoheaters in polymer and biological media: characterization of mechanical destruction and boiling. *Adv Funct Mater* 22: 294–303.

55. Baffou G, Polleux J, Rigneault H, et al. (2014) Super-heating and micro-bubble generation around plasmonic nanoparticles under cw illumination. *J Phys Chem C* 118: 4890–4898.

56. Alaulamie A, Baral S, Johnson S, et al. (2017) Targeted nanoparticle thermometry: A method to measure local temperature at the nanoscale point where water vapor nucleation occurs. *Small* 13: 1601989.

57. Wang Y, Zaytsev M, Lajoinie G, et al. (2018) Giant and explosive plasmonic bubbles by delayed nucleation. *P Natl Acad Sci* 115: 7676–7681.

58. Lachaîne R, Boulais É, Meunier M (2014) From thermo- to plasma-mediated ultrafast laser-induced plasmonic nanobubbles. *ACS Photonics* 1: 331–336.

59. Zhao C, An W, Gao N (2020) Light-induced latent heat reduction of silver nanofluids: A molecular dynamics simulation. *Int J Heat Mass Transf* 162: 120343.

60. Wang Y, Zaytsev M, The H, et al. (2017) Vapor and gas-bubble growth dynamics around laser-irradiated, water-immersed plasmonic nanoparticles. *ACS Nano* 11: 2045–2051.

61. Liu X, Bao L, Dipalo M, et al. (2015) Formation and dissolution of microbubbles on highly-ordered plasmonic nanopillar arrays. *Sci Rep* 5: 18515.

62. Li X, Wang Y, Zaytsev M, et al. (2019) Plasmonic bubble nucleation and growth in water: Effect of dissolved air. *J Phys Chem* 123: 23586–23593.

63. Zhang Q, Neal R, Huang D, et al. (2020) Surface bubble growth in plasmonic nanoparticle suspension. *ACS Appl Mater Inter*, 26680–26687.

64. Setoura K, Ito S, Miyasaka H (2017) Stationary bubble formation and Marangoni convection induced by CW laser heating of a single gold nanoparticle. *Nanoscale* 9: 719–730.

65. Zhao C, Xie Y, Mao Z, et al. (2014) Theory and experiment on particle trapping and manipulation via optothermally generated bubbles. *Lab Chip* 14: 384–391.

66. Czelej K, Colmenares J, Jabłczyńska K, et al. (2021) Sustainable hydrogen production by plasmonic thermophotocatalysis. *Catal Today*, 1–31.

67. Ganeev R, Ryasnyansky A, Kamalov S, et al. (2001) Nonlinear susceptibilities, absorption coefficients and refractive indices of colloidal metals. *J Phys D* 34: 1602–1611.

68. Ashkin A, Dziedzic J, Smith P (1982) Continuous-wave self-focusing and self-trapping of light in artificial Kerr media. *Opt Lett* 7: 276–278.

69. Deng L, He K, Zhou T, et al. (2005) Formation and evolution of far-field diffraction patterns of divergent and convergent Gaussian beams passing through self-focusing and self-defocusing media. *J Opt* 7: 409–415.

70. Nascimento C, Alencar M, Ch'avez-Cerda S, et al. (2006) Experimental demonstration of novel effects on the far-field diffraction patterns of a Gaussian beam in a Kerr medium. *J Opt* 8: 947–951.

71. Setoura K, Werner D, Hashimoto S (2012) Optical scattering spectral thermometry and refractometry of a single gold nanoparticle under CW laser excitation. *J Phys Chem C* 116: 15458–15466.

72. Takeuchi H, Motosuke M, Honami S (2012) Noncontact bubble manipulation in microchannel by using photothermal Marangoni effect. *Heat Transfer Eng* 33: 234–244.

73. Domínguez-Juárez J, Vallone S, Lempel A, et al. (2015) Influence of solvent polarity on light-induced thermal cycles in plasmonic nanofluids. *Optica* 2: 447–453.

74. Juárez J, Vallone S, Moocarme M, et al. (2015) Spontaneous light-driven heat cycles in metallic nanofluids with nanobubbles. *Conf Lasers Electro-Opt*: 1–2.

75. Li Y, Nicolì F, Chen C, et al. (2015) Photoresistance switching of plasmonic nanopores. *Nano Lett* 15: 776–782.

76. Namura K, Nakajima K, Kimura K, et al. (2015) Photothermally controlled Marangoni flow around a micro bubble. *Appl Phys Lett* 106: 043101.

77. Namura K, Nakajima K, Kimura K, et al. (2016) Sheathless particle focusing in a microfluidic chamber by using the thermoplasmonic Marangoni effect. *Appl Phys Lett* 108: 071603.

78. Yan X, Xu J, Meng Z, et al. (2020) A new mechanism of light-induced bubble growth to propel microbubble piston engine. *Small*, e2001548.

79. Li Y, Xu L, Li B (2012) Gold nanorod-induced localized surface plasmon for microparticle aggregation. *Appl Phys Lett* 101: 053118.

80. Zheng Y, Liu H, Wang Y, et al. (2011) Accumulating microparticles and direct-writing micropatterns using a continuous-wave laser-induced vapor bubble. *Lab Chip* 11: 3816–3820.

81. Fang N, Lee H, Sun C, et al. (2005) Sub-diffraction-limited optical imaging with a silver superlens. *Science* 308: 534–537.

82. Atwater H, Polman A (2010) Plasmonics for improved photovoltaic devices. *Nat Mater* 9: 205–213.

83. Kabashin A, Evans P, Pastkovsky S, et al. (2009) Plasmonic nanorod metamaterials for biosensing. *Nat Mater* 8: 867–871.

84. Xiao S, Drachev V, Kildishev A, et al. (2010) Loss-free and active optical negative-index metamaterials. *Nat Commun* 466: 735–738.

85. Gan F, Wang Y, Sun C, et al. (2017) Widely tuning surface plasmon polaritons with lase' induced bubbles. *Adv Opt Mater* 5: 1600545.

86. Daniel M, Astruc D (2004) Gold nanoparticles: assembly, supramolecular chemistry, quantum-size-related properties, and applications toward biology, catalysis, and nanotechnology. *Chem Rev* 104: 293–346.

87. Zohdy M, Tse C, Ye J, et al. (2006) Optical and acoustic detection of laser-generated microbubbles in single cells. *IEEE T Ultrason Ferr* 53: 117–125.

88. Dadwal A, Baldi A, Narang R (2018) Nanoparticles as carriers for drug delivery in cancer. *Artif Cells Nanomed Biotechnol* 46: 295–305.

89. Wan W, Yang L, Padavan D (2007) Use of degradable and nondegradable nanomaterials for controlled release. *Nanomedicine* 2: 483–509.

90. Sinha R, Kim G, Nie S, et al. (2006) Nanotechnology in cancer therapeutics: bioconjugated nanoparticles for drug delivery. *Mol Cancer Ther* 5: 1909–1917.

91. Veiseh O, Gunn J, Zhang M (2010) Design and fabrication of magnetic nanoparticles for targeted drug delivery and imaging. *Adv Drug Deliv Rev* 62: 284–304.

92. Anderson L, Hansen E, Lukianova-Hleb E, et al. (2010) Optically guided controlled release from liposomes with tunable plasmonic nanobubbles. *J Control Release* 144: 151–158.

93. Huang WT, Chan M, Chen X, et al. (2020) Theranostic nanobubble encapsulating a plasmon-enhanced upconversion hybrid nanosystem for cancer therapy. *Theranostics* 10: 782–796.

94. Lukianova-Hleb E, Hanna E, Hafner J, et al. (2010) Tunable plasmonic nanobubbles for cell theranostics. *Nanotechnology* 21: 85102.

95. Liu Y, Ye H, Huynh H, et al. (2021) Single-particle counting based on digital plasmonic nanobubble detection for rapid and ultrasensitive diagnostics. *medRxiv: the preprint server for health sciences*.

96. Wagner D, Delk N, Lukianova-Hleb E, et al. (2010) The in vivo performance of plasmonic nanobubbles as cell theranostic agents in zebrafish hosting prostate cancer xenografts. *Biomaterials* 31: 7567–7574.